International Journal of Pharmaceutics 667 (2024) 124951

Contents lists available at ScienceDirect

International Journal of Pharmaceutics

journal homepage: www.elsevier.com/locate/ijpharm

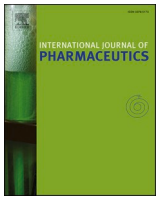

Development of a hybrid CuS-ICG polymeric photosensitive vector and its application in antibacterial photodynamic therapy

Cristina Yus [a,b,d,*], Teresa Alejo [a,b,c,d], Cristina Quílez [e,f,*], Silvia Irusta [a,b,d], Diego Velasco [e,f], Manuel Arruebo [a,b,d], Victor Sebastian [a,b,c,d]

[a] Department of Chemical Engineering. University of Zaragoza, Campus Río Ebro-Edificio I+D, C/ Poeta Mariano Esquillor S/N, Zaragoza 50018, Spain
[b] Instituto de Nanociencia y Materiales de Aragón (INMA), CSIC-Universidad de Zaragoza, Zaragoza 50009, Spain
[c] Networking Research Center on Bioengineering, Biomaterials and Nanomedicine, CIBER-BBN, Madrid 28029, Spain
[d] Aragon Health Research Institute (IIS Aragon), Zaragoza 50009, Spain
[e] Department of Bioengineering, Universidad Carlos III de Madrid, Leganés 28911, Spain
[f] Fundación Instituto de Investigación Sanitaria de la Fundación Jiménez Díaz, Madrid 28040, Spain

ARTICLE INFO

Keywords:
Antimicrobial photodynamic therapy
Indocyanine green
Nanoparticles
Copper sulphide
MRSA
Skin substitutes
Wound Healing

ABSTRACT

At the present time, owing to the extremely high growth of microbial resistance to antibiotics and, consequently, the increased healthcare associated costs and the loss of efficacy of current treatments, the development of new therapies against bacteria is of paramount importance. For this reason, in this work, a hybrid synergetic nanovector has been developed, based on the encapsulation of a NIR (near infrared) photosensitive molecule (indocyanine green, ICG) in biodegradable polymeric nanoparticles (NPs). In addition, copper sulfide nanoparticles (CuS NPs), optically sensitive to NIR, were anchored on the polymeric nanoparticle shell in order to boost the generation of reactive oxygen species (ROS) upon NIR irradiation. As a result, the nanohybrid synthesized material is capable to generate ROS on demand when exposed to a NIR laser (808 nm) allowing for the repeated triggering of ROS production upon NIR light exposure. After each irradiation, the ROS generated were able to eliminate pathogenic bacteria, as it was demonstrated *in-vitro* with three bacterial strains, *Staphylococcus aureus* ATCC 25923 used as a reference strain *(S. aureus*), *S. aureus* USA300 (methicillin-resistant strain, MRSA) and GFP-expressing antibiotic-sensitive *S. aureus* (methicillin-sensitive strain, MSSA). Finally, the effect of the hybrid NPs in the skin bed was tested on a plasma-derived *in vitro* skin model. Fluorescence and histological images showed the presence of CuS NPs all over the dermal layer lacking epidermis of the skin construct. Thus, the *in vitro* model facilitated the prediction of the nanovector's behavior in a human skin equivalent, showcasing its potential application against topical infections after wounding.

1. Introduction

The excessive and uncontrolled use of antibiotics not only in humans but also in farming, crops and aquaculture is resulting in the global threat of antimicrobial resistance. The misuse of antibiotics and the spontaneous bacteria mutations are showing that some antibiotics that were effective against a certain strain, are no longer effective against the same strain (Thapa et al., 2020). To be even more discouraging, the lack of new antibiotics is undermining the past efforts to fight bacterial infections and microbial resistance (Piksa et al., 2023). At the end, the microbial resistance is associated with an increase of healthcare expenditures (surgery, long hospital stay…), and in some cases it could even increase the mortality in cases of incurable bacterial infections (Sipahi, 2008).

Antimicrobial Photodynamic Therapy (aPDT) is being considered a promising alternative way of eliminating bacteria since bactericidal efficiency is independent of the antibiotic resistance pattern. aPDT requires the presence of an exogenous light-activated molecule (photosensitizer) in the presence of tissue oxygen and a harmless low-intensity light source to promote the formation of reactive oxygen species (ROS) that generate a lethal oxidative stress to bacteria. This therapeutic approach is minimally invasive but it is very sensitive to the

* Corresponding authors at: Department of Chemical Engineering. University of Zaragoza, Campus Río Ebro-Edificio I+D, C/ Poeta Mariano Esquillor S/N, Zaragoza 50018, Spain (C. Yus); Department of Bioengineering, Universidad Carlos III de Madrid, Leganés 28911, Spain (C. Quílez).
E-mail addresses: cyargon@unizar.es (C. Yus), cquilez@ing.uc3m.es (C. Quílez).

https://doi.org/10.1016/j.ijpharm.2024.124951
Received 25 July 2024; Received in revised form 7 November 2024; Accepted 11 November 2024
Available online 14 November 2024

photosensitizer stability since this molecule is the ROS promotor. Photosensitizers should be ideally activated by a light source in the therapeutic NIR window of 650–900 nm because these wavelengths enhance penetration depth and minimize tissue light absorption. The ROS generated can be classified in two types depending on the formation mechanism: Type I, derived from free radicals and Type II, resulted from singlet oxygen. Interestingly, the development of bacterial resistance toward radicals Type I and specially against Type II is highly unlikely (Magadla et al., 2019). A variety of organic and inorganic photosensitizers has been developed to treat Gram-positive (gram +) and Gram-negative (gram −) bacteria (Garin et al., 2021),(Ghorbani et al., 2018). Photofrin® was the first photosensitizer to receive regulatory approval for the treatment of bladder cancer (Rahman et al., 2023). There are many molecules that exhibit photosensitizing properties, but very few have made it to clinical trials and are commercially available (Garapati et al., 2023). A first and second generation of photosensitizers have been developed, but a third generation of photosensitizers was created to address the shortcomings of previous molecules, such as poor clearance and high dark cytotoxicity due to low absorption bands at NIR wavelengths or the low tissue selectivity, causing severe skin photosensitivity (Garapati et al., 2023). This new generation is based on the conjugation of photosensitizers to antibodies or nanoparticles to increase bioavailability, retention and penetration of the photosensitizer in the target cell and to improve both water solubility and lifetime.

It has been reported that the ROS generated are responsible to kill bacteria following two mechanisms: affecting the cell membrane or damaging the molecular cytoplasmic components (DNA, enzymes or proteins) (Alves et al., 2014). Normally, the main structures that are damaged by this therapy are the external ones since high concentrations of internalized photosensitizers must be reached for intracellular damage (Cieplik et al., 2018). Consequently, the response of the aPDT mainly depends on the proximity of the photosensitive molecule to the targeted bacterial cells or its internalization, it means that the chemical properties of the molecule (superficial charge, stability, etc.) are going to be crucial (Youf et al., 2021). The importance of its spatial location is due to the fact that the closer the photosensitizer is to the target; the better the antimicrobial efficacy observed. The main reason is the especially short half-life of the ROS (in the μs range) and the average reduced distance of action (less than 1 μm) (Cieplik et al., 2018). Therefore, as a consequence of the multi-targeting, non-specificity of the ROS damage produced by light-excited photosensitizers and their quick action, the probability of apparition of bacterial resistances seems to be reduced (Maisch, 2015).

The human body is entirely covered by skin and as a part of its protective function it is exposed to injuries (Kolarsick et al., 2011), (James et al., 2019). This function relies mainly on the complex composition and structure of its outer most layer, the epidermis, which hinders the entrance of foreign substances and organisms to the inner body (Proksch et al., 2008). During the past two decades, bilayered plasma-derived fibrin skin substitutes harboring primary dermal fibroblasts and epidermal keratinocytes have been used in different applications: 1) to treat patients with extensive burns and traumatic/surgical wounds (Llames et al., 2004),(Llames et al., 2006),(Gómez et al., 2011); 2) to generate skin humanized mouse models (Guerrero-Aspizua et al., 2010),(Martínez-Santamaría et al., 2013),(Carretero et al., 2016); 3) to develop a complete 3D printed bilayered system used for clinical and commercial testing purposes (Cubo et al., 2016); and 4) to generate complex anatomically and physiologically relevant *in vitro* skin models (Quílez et al., 2024). In this case, the dermal compartment is generated by the polymerization of fibrinogen (contained in blood plasma) into the fibrin clot to mimic the first stage of the wound healing process, which is further cultured to promote the deposition of type I collagen by the embedded fibroblasts to obtain a mature skin construct (Mazlyzam et al., 2007). This fact, grants the skin construct with a dual application to be used either as wound or healthy skin model in the early and mature stages, respectively, a feature that is not available for the widely used collagen-based skin constructs (Randall et al., 2018).

In our previous work (Garin et al., 2021), we proposed the combination of two photosensitizers, the FDA approved indocyanine green (ICG) with chalcogenide nanoparticles based on copper sulfide (CuS). Although CuS NPs are inorganic, they are able to biodegrade to copper sulfates (Ortiz De Solorzano et al., 2016), so both photosensitizers are finally biodegradable, avoiding their cellular accumulation. The proposed combination of photosensitizers is NIR-light triggerable to reach deeper skin penetration and increase ROS generation efficiency while avoiding unwanted water and hemoglobin light attenuation. In this case, a synergetic antimicrobial photodynamic activity resulted from the combination of those two different photosensitizers where each one efficiently generated ROS at different levels: 1) ICG in the cellular cytosol due to its easy diffusion and 2) CuS NPs in the extracellular space due to their nanometric size.

Considering our previous results and the aforementioned advantages of conjugating photosensitizers with nanoparticles, herein, we have developed a novel antimicrobial photodynamic hybrid vector based on the synergetic benefits of: 1) encapsulating ICG inside a biodegradable polymeric nanoparticle to improve ROS production (mainly singlet oxygen) (Shirata et al., 2017) by decreasing photobleaching and aggregation and 2) linking CuS nanoparticles to the surface of the biodegradable polymeric nanoparticle to increase the ROS production (mainly peroxide, hydroxyl and hypochlorite) (Li et al., 2017) and take advantage of the cooper antibacterial activity, as it has been reported in our previous research (Garin et al., 2021). In this work, we demonstrate the effective *in vitro* antimicrobial activity of the developed NIR-light excitable nanoparticles against three bacterial strains: *Staphylococcus aureus* (*S. aureus*) ATCC 25923, methicillin-resistant *S. aureus* USA300 (USA300 MRSA) in planktonic form and methicillin-sensitive GFP-expressing antibiotic-sensitive *S. aureus* (*S. aureus* GFP) in biofilm form. Moreover, a histological study and the permeability through the skin were tested *in vitro* with dermo-epidermal skin equivalents concluding that a total absence of significant histological modifications was observed and that only the damaged skin lacking epidermis is permeable to the particles. This fact suggests that the photodynamic treatment can act deeper on the infected wound bed and unwanted photodynamic effects can be prevented on healthy intact skin.

2. Materials and methods

2.1. Materials

Polymers PLGA ester terminated (50/50 Poly (D, L-lactide-co-glycolide), molecular weight 38–54 kDa, under the commercial name Resomer® RG 504, and Eudragit® RS100 (RS), were purchased from Evonik Industries AG (Darmstadt, Germany). Acetone (+99 %) was supplied by Fisher Scientific (Waltham, Massachusetts, USA), indocyanine green (USP Reference Standard), surfactant Pluronic® F-68, copper chloride dihydrate ($CuCl_2{\cdot}2H_2O$), sodium sulfide nonahydrate ($Na_2S{\cdot}9H_2O$), polyvinylpyrrolidone K30 (PVP) and bovine serum albumin (BSA) were supplied by Sigma-Aldrich (St. Louis, MO, USA). All the reagents were used without further purification.

2.2. Production of nanoparticles of RS-PLGA-ICG@CuS nanoparticles

2.2.1. RS-PLGA-ICG nanoparticles synthesis

Polymeric NPs (PLGA and RS-PLGA NPs) were prepared by a nanoprecipitation and solvent evaporation procedure, according to a modification of the synthesis of Yurtdaş-Kırımlıoğlu et al. (Yurtdaş-Kırımlıoğlu and Görgülü, 2021) and here briefly described. An organic solution (3 mL) of PLGA (50 mg) or PLGA (25 mg) and RS (25 mg) in acetone was added dropwise into 10 mL of an aqueous solution containing 0.5 % (w/v) of Pluronic® F68 using a syringe pump (Harvard Apparatus, Holliston, MA, USA) at a flow rate of 0.5 mL/min. After polymer nanoprecipitation, the organic solvent was evaporated under

magnetic stirring for 4 h at room temperature. The aqueous suspension of NPs was purified by centrifugation (7500 rpm, 10 min). The supernatant was centrifuged at 13000 rpm for 10 min. The pellets were resuspended in MilliQ-H_2O. 10 % (w/v) of BSA was added to the suspension of NPs to prevent their agglomeration. NPs were stored at 4 °C until required. For ICG encapsulation, different quantities of ICG (10, 7.5, 5, 2.5 % (w/w) referred to the total polymer) dissolved in DMSO were added to the organic solution and the nanoprecipitation process was performed as aforementioned described, but protecting the colloid from light using aluminum foil.

2.2.2. Ultrasmall CuS nanoparticles synthesis

CuS nanoparticles (CuS NPs) synthesis was carried out following the previous work of Liu et al. (Liu et al., 2015) with some modifications to better control the particle size distribution. Briefly, 180 mL of 0.185 mg/mL $CuCl_2$ and 200 mg of PVP were mixed for 30 min under magnetic stirring. Then, 20 mL of Na_2S aqueous solution (2.4 mg/mL) was added dropwise. After that, the yellow-colored solution was heated at 90 °C for 30 min under continuous stirring, until the solution turned dark-green. Finally, the NPs were cooled down to room temperature. Several washing cycles were carried out by centrifugation using Amicon® Ultra-15 Centrifugal Filters (100 KDa) for 10 min at 5500 rpm. The final dispersion was kept at 4 °C until needed.

2.2.3. RS-PLGA@CuS and RS-PLGA-ICG@CuS hybrid nanoparticles synthesis

The interaction between RS-PLGA or RS-PLGA-ICG NPs and CuS NPs was carried out via electrostatic interactions. Different quantities of CuS NPs were mixed with the polymeric NPs. The studied ratios were 1:5, 1:1, 1:0.5, 1:0.1 and 1:0.05. The mixed NPs were kept at 4 °C in the dark without stirring for 1 h. After that time, free unbound CuS NPs were removed by centrifugation (10 min, 7500 rpm) three times. 10 % (w/v) of BSA was added to the suspension of RS-PLGA@CuS NPs and RS-PLGA-ICG@CuS NPs to prevent agglomeration.

2.3. Characterization of the nanoparticles

Size, morphology and shape characterization of produced NPs were carried out using electron microscopy analysis. An Inspect F50 field emission gun scanning electron microscope (SEM, FEI Company, Eindhoven, the Netherlands) at 10 kV was used to study the nanoparticle shape and morphology. Samples were previously sputtered with a coating of Pd (Leica EM ACE200, Wetzlar, Germany). A T20-FEI transmission electron microscope (TEM, FEI Company, Eindhoven, The Netherlands) and a high-angle annular dark-field scanning transmission electron microscopy (HAADF-STEM, FEI Company, Eindhoven, The Netherlands) were used to characterize the NPs size. TEM samples were prepared by depositing 20 μL of NPs dispersed in MilliQ-H_2O onto a TEM grid and then dried overnight. The particle size distribution histogram was calculated measuring the NPs diameter of the resulted TEM images with the ImageJ software and using statistical analysis (particles measured for statistical analysis N = 150).

Hydrodynamic particle size was measured by Dynamic Light Scattering (DLS, Zeta Plus; Brookhaven Instruments Corporation, Holtsville, NY, USA). NPs were diluted in MilliQ-H_2O and the size parameters were determined at 25 °C. Surface charge was measured by Z-potential (Zeta Plus; Brookhaven Instruments Corporation, Holtsville, NY, USA). NPs were diluted in a KCl buffer solution to provide constant ionic strength at pH 6. At least three different samples were measured.

To determinate the amount of ICG encapsulated, 10 μL of the resulting NPs were dissolved in DMSO and the ICG contained was measured by UV–Vis spectrophotometry (Jasco V670, Jasco Applied Science, Eschborn, Germany) at a wavelength of 794 nm. At least three different samples were measured to obtain statistical significance. Previously, a calibration curve was performed from 0 to 2.5 ppm of ICG. Encapsulation efficiency (EE) and drug loading (DL) were determined using the following equations:

$$\text{EE } (\%) = \frac{\text{weight ICG measured(mg)}}{\text{weight ICG added(mg)}} \text{ x } 100 \quad (1)$$

$$\text{DL } (\%) = \frac{\text{weight ICG measured (mg)}}{\text{weight of ICG loaded NPs(mg)}} \text{ x } 100 \quad (2)$$

An energy-dispersive X-ray (EDS, Inspect F50 SEM) analysis confirmed the presence of CuS and Cu/S ratios were also quantified. X-ray photoelectron spectroscopy (XPS, Axis Ultra DLD, Kratos Tech., Manchester, UK) was used to determine the oxidation state of the CuS NPs and the Cu/S ratios. The crystallinity and structure of the CuS NPs were analyzed by X-ray diffraction (XRD, Empyrean, Malvern Panalytical, Malvern, UK) ranging from 20 to 70 degrees.

The amount of Cu incorporated onto the surface of the RS-PLGA@CuS NPs and RS-PLGA-ICG@CuS NPs was determined by using a Microwave Plasma Atomic Emission Spectrometer (Agilent Technologies, Santa Clara, USA). Samples were previously digested with a mixture of aqua regia and distilled water (1:5) and filtered using a 0.2 μm filter. Thermogravimetric analysis (TGA, Mettler Toledo, L'Hospitalet de Llobregat, Barcelona, TGA/SDTA 851e) of RS-PLGA-ICG@CuS NPs was also performed to corroborate the amount of CuS NPs incorporated onto the surface of the polymeric NPs. The TGA measurements were conducted in a nitrogen atmosphere at a heating rate of 10 °C/min, covering a temperature range from 30 to 800 °C.

Fourier-transform infrared (FTIR) spectra were recorded to evaluate if any molecular interactions occured between ICG and the polymers. Spectra were obtained using a Bruker VERTEX 70 FTIR spectrometer (Bruker, Billerica, MA, USA) equipped with a Golden Gate diamond ATR accessory, recorded by averaging 40 scans in the 4000 – 600 cm^{-1} wavenumber range at a resolution of 4 cm^{-1}. Data evaluation was carried out using the OPUS software from Bruker Optics.

2.4. In vitro ICG and CuS NPs stability study

In order to study the effect of ageing time and temperature on the absorbance stability of ICG and CuS NPs different solutions of free ICG, RS-PLGA-ICG NPs and CuS NPs were prepared and stored at 4 °C and 37 °C over time. UV–Vis absorbance measurements at predetermined time intervals (0, 1, 2, 3, 5 and 10 days) were performed.

2.5. In vitro ICG release study

The *in vitro* release of ICG was performed under sink conditions by introducing the NPs at a concentration of 1 mg/mL in PBS 1x and in MilliQ-H_2O, separately. NPs were incubated at 37 °C under continuous mixing, and at predetermined time intervals (0, 2, 4, 6, 24, 48 and 72 h), NPs were centrifuged (10 min at 13,300 rpm) and the supernatant was discarded. The pellet was dissolved in 1 mL of DMSO and the ICG amount retained into the particles was measured by UV–Vis at a wavelength of 794 nm. The released ICG was calculated according Eq.3:

$$\text{Released ICG} = \frac{\text{weight (encapsulated ICG-retained ICG), mg}}{\text{weight (encapsulated ICG), mg}} \text{ x } 100 \quad (3)$$

In this particular case, the retained ICG into the NPs was preferentially measured instead of the released ICG to avoid the necessary correction because of the degradation of the released ICG in aqueous solutions at 37 °C.

2.6. Photothermal study in aqueous solution

Photothermal effects of free ICG solution, RS-PLGA-ICG NPs and RS-PLGA-ICG@CuS hybrid NPs in water were measured. The aqueous dispersions were irradiated with an 808 nm wavelength laser diode (6 x 8

mm^2 spot size; Optilas model MDL-III-808–2 W, Changchun New Industries Optoelectronics Technology Co., Ltd, Changchun, China) using an irradiance of 1 W/cm^2. Temperature increase was monitored using a K-type thermocouple (RS Amidata, Madrid, Spain) to decouple photothermal from photodynamic effects.

2.7. ROS determination

To detect reactive oxygen species (ROS) generated by the hybrid NPs under light irradiation, dihidrorhodamine 123 (DHR123, Sigma-Aldrich, St. Louis, MO, USA) was used. The non-fluorescent probe DHR123 is oxidized in the presence of ROS forming a fluorescent molecule rhodamine 123 (R123), with an emission peak at 530 nm based on our prior findings (Paesa et al., 2023). Briefly, the ICG solution (100 ppm), RS-PLGA@CuS NPs and RS-PLGA-ICG@CuS NPs dispersions (at the concentration needed to reach 100 ppm of encapsulated ICG) and a dispersion of CuS NPs at the same concentration as the CuS NPs anchored on the surface of the polymeric particles, were incubated at 37 °C under continuous shaking. At different time points (24, 48 and 72 h) the dispersions were irradiated at 1 W/cm^2 for 5 min using an 808 nm laser, the same conditions used for bacterial assays. To measure the ROS production at each time point, the stock solution of DHR123 prepared in DMSO was mixed to reach a final concentration of 40 μM. The formation of R123, with and without light application, was monitored at 530 nm using an excitation wavelength of 485 nm measured with a fluorimeter (Varioskan LUX multimode microplate reader, Thermo Fisher Scientific, USA). The experiments were conducted under dark conditions to verify ROS generation only upon the irradiation of NIR light to the suspensions.

2.8. In vitro antibacterial photodynamic therapy

2.8.1. Bacterial isolates and culture conditions

S. aureus ATCC 25923 used as a reference strain (*S. aureus*), obtained from Ielab (Spain), GFP-expressing antibiotic-sensitive *S. aureus* (*S. aureus* GFP) and a clinical methicillin-resistant strain (USA300 MRSA), kindly donated by Dr. Cristina Prat, Institut d'Investigació en Ciencies de la Salut Germans Trias i Pujol (IGTP, Spain) were used in the experiments as models of pathogenic bacteria commonly infecting skin and soft tissues. All the strains were seeded on tryptone soya agar (TSA, Conda-Pronadisa S.A., Torrejón de Ardoz, Spain) at 37 °C in aerobic conditions. A colony of each strain was cultured in tryptone soya broth (TSB, Conda-Pronadisa S.A., Spain) and incubated at 37 °C under aerobic conditions until stationary growth was reached. Then, bacteria were diluted to 10^6 CFU/mL in TSB.

2.8.2. Bactericidal photodynamic therapy assay

100 μL of *S. aureus* and USA300 MRSA bacteria (10^6 CFU/mL) and 100 μL of free ICG, RS-PLGA-ICG NPs or RS-PLGA-ICG@CuS NPs, prepared twice at selected concentrations and previously sterilized under UV light, were added into Eppendorf tubes. The ICG concentrations assayed were 50 and 100 ppm. The polymeric NPs concentrations were the needed to reach the same ICG encapsulated concentration as the free ICG concentrations tested. Bacteria and the corresponding treatment suspensions were kept at 37 °C under aerobic conditions 24 h. After this incubation, samples were irradiated at 1 W/cm^2 for 5 min, corresponding to the 24 h time point. The irradiation was repeated after 48 and 72 h of incubation (48 and 72 h time points, respectively). At all the time points studied, 15 min after irradiation, viable bacteria were counted by the serial dilution method. RS-PLGA NPs (without ICG and CuS NPs) were assayed as control, as well as laser irradiation without NPs to prove that only the NIR exposure does not produce any antimicrobial effect. Bacteria culture in only TSB was used as positive control. At least three independent assays were performed in duplicate.

After photodynamic treatment, bacteria morphology was evaluated by SEM as previously reported (Mendoza et al., 2017). Briefly, after 5 min of 808 nm laser irradiation, bacteria were centrifuged 5 min at 3,000 rpm and fixed with 4 % paraformaldehyde in PBS (PFA, Alfa Aesar, USA.) overnight. Then, fixed bacteria were washed with DDI water. Dehydration with ethanol was not carried out to prevent the dissolution of the RS particles. Before the visualization, bacteria samples were dried at room temperature and coated with Pd, as mentioned.

2.8.3. Antibiofilm photodynamic therapy assay

GFP *S. aureus* was cultured in TSB and incubated at 37 °C under aerobic conditions until stationary growth was reached. Then, bacteria were diluted to 10^5 CFU/mL and 2 mL of diluted cultures were added to ibiTreat plates (μ-dish 35 mm) and incubated at 37 °C without shaking for 24 h. When the biofilm was formed, planktonic cells were removed and wells were gently washed with PBS, then, RS-PLGA-ICG@CuS NPs were added to the culture and incubated for 24 h. After that time of incubation, biofilms were irradiated (808 nm, 1 W/cm^2, 5 min) and prepared for confocal microscopy. Briefly, the biofilm was stained with calcofluor white stain for 1 min and, after washing the biofilm twice with PBS, 4 % PFA solution in PBS was added and incubated for 30 min. Then, samples were prepared for visualization by confocal microscopy (Confocal Zeiss LSM 880 with Airyscan) in Fluoromount mounting medium. Non-irradiated biofilm treated with RS-PLGA@ICG-CuS NPs and biofilm without any treatment were visualized as controls.

2.9. Permeability assay using in vitro dermo-epidermal skin equivalents

To study the effect of the RS-PLGA-ICG@CuS NPs on the artificial skin, plasma-based *in vitro* dermo-epidermal skin equivalents at a final fibrin concentration of 2.4 mg/mL were generated using both primary human fibroblasts and keratinocytes according to the previously described protocol (Montero et al., 2021). After 15 days in culture in the air–liquid interface, the epidermis of the organotypic skin cultures was correctly differentiated, time at which they were ready to be used in the NPs skin permeation test. To analyze the role of the epidermis, two experiments were carried out in parallel: *in vitro* skin with and without the epidermis. For the later, once the *in vitro* skin cultures were ready to be used, the epidermis was carefully removed with the help of precision clamps.

To determine the NPs skin permeability, *in vitro* skin tests were performed adding 500 μL of the RS-PLGA-ICG@CuS NPs dispersion on top of the skin cultures with and without epidermis. The culture media below the insert culture plates were removed and replaced by PBS 1X modified without calcium chloride and magnesium chloride (Sigma-Aldrich, USA). *In vitro* skin constructs were cultured at 37 °C and 5 % CO_2. To study the permeation of the NPs, 1 mL sample of the PBS 1X was extracted at different timepoints (0, 1, 4, 6 and 24 h) for further analysis. For each condition, three independent samples were analyzed. Ionic copper (Cu^{2+}) permeation determination through the corresponding skin substitute was carried out using ICP-MS, after digestion of 200 μL of each sample in aqua regia for 24 h.

Finally, assayed skins were removed from the culture insert. Samples were divided in two using a scalpel, one half of the sample was fixed and paraffin-embedded for histological analysis using H&E and the other half was embedded in OCT tissue fixative for cryosection and visualization under a confocal microscope (Confocal Zeiss LSM 880, Zeiss, Germany) in the scientific-technical service of microscopy and imaging (IACS-Universidad de Zaragoza, Spain).

2.10. Statistical analysis

All data were expressed as the mean ± standard deviation (SD). Statistical analysis was performed using GraphPad Prism 8 software (GraphPad Software Inc., USA) using a two-way analysis of variance (ANOVA) set for multiple comparisons with a Dunnett's test. When $p \leq 0.05$ statistically significant differences were considered. Each experiment was performed in triplicate.

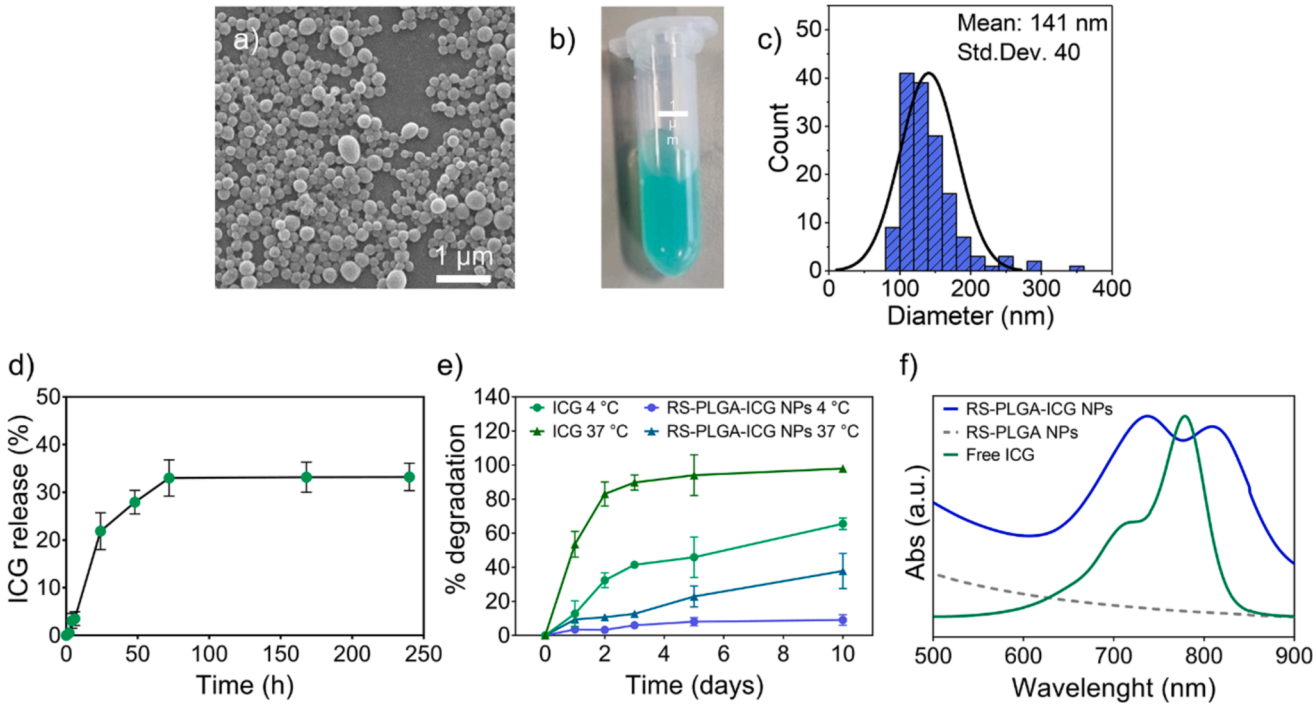

Fig. 1. a) SEM image of the RS-PLGA-ICG NPs, b) image of an aqueous suspension of the RS-PLGA-ICG NPs, c) size distribution of RS-PLGA-ICG NPs obtained from the SEM measurements (N = 150), d) ICG release profile from RS-PLGA-ICG NPs, e) free ICG and encapsulated ICG stability study and f) UV–Vis spectra in arbitrary units (a.u.) of free ICG, RS-PLGA NPs and RS-PLGA-ICG NPs.

3. Results and discussion

The synthesis of the hybrid NPs was performed in two steps. Firstly, the polymeric NPs (PLGA, RS-PLGA and RS-PLGA-ICG NPs) were prepared by nanoprecipitation, followed by electrostatic bonding with separately prepared CuS NPs.

PLGA polymer was selected because it is known for its high biocompatibility, it can be hydrolyzed into lactic and glycolic acids, metabolites of the cellular cycle, offering also sustained release, and because it is approved by the FDA as composing material in many medical devices and drug delivery systems (Makadia and Siegel, 2011). PLGA NPs were synthesized and their representative size analysis is depicted in Figure S1. The Z-potential of PLGA NPs was negative (−26.5 ± 1.2 mV) at pH 6. However, a positive Z-potential should be required to confer electrostatic interaction between the polymeric NPs and the negatively charged CuS NPs. The need of conferring a positive charge on PLGA surface was addressed by using a combination of PLGA and the positive charged RS polymer due to the presence of positive charged quaternary ammonium groups in the latter (Yus et al., 2020). A representative SEM image of the empty polymeric RS-PLGA NPs is depicted in Figure S1. The colloid of empty RS-PLGA NPs exhibits an average size of 170 ± 60 nm (N = 150), and a Z-potential of 45.7 ± 4.3 mV (Figure S1). Due to the reversal of the surface charge of the NPs after adding the RS polymer, it can be elucidated that RS was successfully incorporated into the NPs. Finally, the effective diameter of PLGA NPs was increased when RS polymer was added (Figure S1), probably due to the different viscosity of the organic solution due to the mixture of both polymers.

ICG encapsulation was limited by the insolubility of the molecule in different organic solvents. Finally, a 5 % (w/w) respect to the polymer in DMSO was selected as the ideal condition of encapsulation, preventing the precipitation of the polymers. When ICG was encapsulated, the uniform particle size distribution measured from SEM images was 141 ± 40 nm (Fig. 1a-c), and the stable colloidal solution is presented in Fig. 1b. The Z-potential was reduced to 27.3 ± 1.35 mV, compared to that of unloaded NPs, but still having enough positive charge to be able to attach negatively charged CuS NPs by supramolecular interactions. The reduction of the Z-potential is probably attributed to the electrostatic interaction between the ICG molecules and the positively charged polymeric particles. The ICG loading ratio was 0.9 ± 0.1 %, the encapsulation efficiency was 6.6 ± 1.2 % and the yield of the synthesis was 39.4 ± 3.5 %. As far as we know, there are no evidences in the previous literature of the encapsulation of ICG in nanoparticles composed of the mixture of these two polymers (RS-PLGA). However, there are some studies where the ICG has been encapsulated in PLGA NPs presenting drug loading values lower than those reported here. Some of these studies were the reported by Ma et al. (Ma et al., 2012), where the ICG loading was 0.21 %, or by Saxena et al. (Saxena et al., 2004) who reported a loading of 0.17–0.29 % (w/w). Other bioactive molecules can be found encapsulated into RS-PLGA NPs, such as the antibiotic ciprofloxacin reported by Dillen et al. (Dillen et al., 2006) where the authors achieve an encapsulation efficiency between 60 and 70 %. The loading of the antifungal nystatin into RS-PLGA NPs, with RS:PLGA ratio of 1:1, was also reported by Mohammadi et al. (Mohammadi et al., 2017), showing an encapsulation efficiency of 47.58 ± 2 %, superior to those obtained in this work, probably due to the structural differences and chemical natures of the different encapsulated molecules.

The ICG release study is presented in Fig. 1d. After 72 h under sink conditions in PBS 1x the 33 ± 4 % of the ICG was released showing an initial burst release (21.9 ± 3.9 % of the loaded amount was released in the first 24 h) and followed by a prolonged sustained release over time. This behavior is in accordance with the observations by other authors who have reported that the drug release from PLGA is higher than that from the RS and PLGA mixture, probably because more compact polymeric particles resulted when two different polymers were combined and to the possible interactions between both polymers creating a robust matrix and hindering the diffusion of the entrapped molecules to the release medium (Dillen et al., 2006),(Hoffart et al., 2002).

The stability study of ICG aqueous solution showed an absorbance drop by almost half in only 24 h at 37 °C and nearly 90 % after 72 h at 37 °C due to the hydrolysis and photobleaching of the molecule as previously reported (Saxena et al., 2003),(Shan et al., 2018). Whereas the encapsulated ICG displayed 10 % degradation in 24 h at 37 °C and

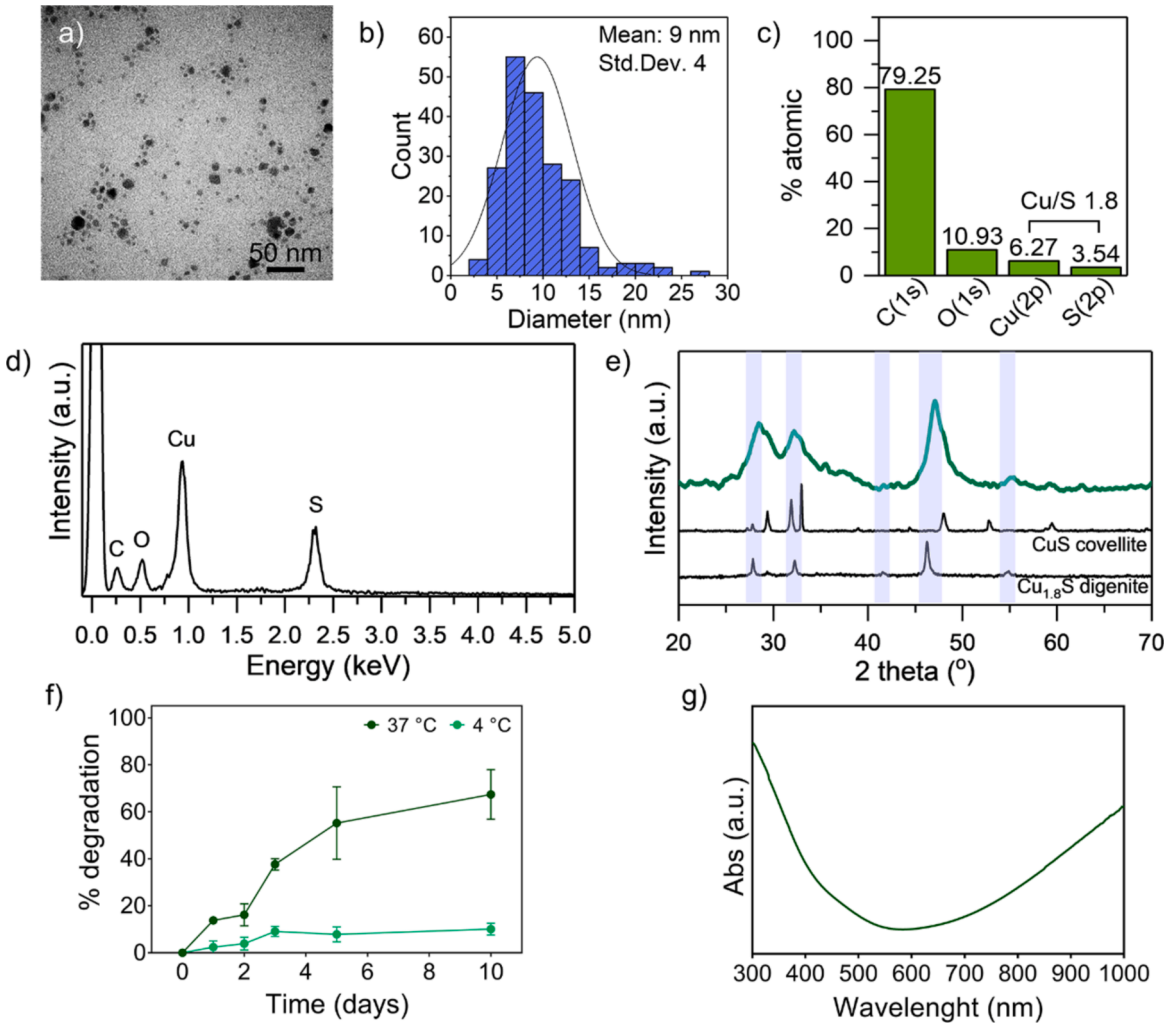

Fig. 2. CuS NPs physico-chemical characterization: a) TEM image of CuS NPs, b) size distribution obtained from TEM measurements (N = 150), c) XPS analysis, d) EDS spectrum, e) XRD analysis and ICDD patterns for covellite and digenite, f) thermal stability study and g) UV–Vis spectrum of CuS NPs.

13 % after 72 h at the same conditions (Fig. 1e). These results confirm the long-term protection of the ICG molecules encapsulated in the polymeric NPs produced in this work. Fig. 1f showed the UV–Vis absorption of free and encapsulated ICG. Comparing the spectra of free and encapsulated ICG, a red shift of 30 nm of the main absorption peak was revealed, which confirms the interaction between the ICG and the encapsulating polymers.

The inorganic ultrasmall CuS NPs synthesized in aqueous solution in this work yielded a narrow size distribution centered at 9 ± 4 nm (Fig. 2a-b). Both, XPS analysis (Fig. 2c) and XRD diffraction peaks (Fig. 2e) suggested that the crystalline phase of the particles corresponds to digenite-phase ($Cu_{1.8}S$) (Lafuente et al., 2016). In the XRD spectra, the peaks corresponding to the XRD patterns of the corresponding phases with which they were matched are highlighted as shaded areas to favor their identification. Fig. 2d shows the EDS spectrum of the CuS NPs where only Cu and S are present together with organic C and O from the polymer. CuS NPs showed high stability when kept at 4 °C, with only a 10.8 ± 2.5 wt.% of degradation in 10 days. Though, Fig. 2f shows that more than 60 % of the NPs were degraded in 10 days when kept at 37 °C. This is a positive outcome considering a potential biological application to avoid any metal bioaccumulation after use. The same results were obtained in previous works where the plasmonic absorption was reduced over time and the degradation of the nanoparticles was increased at higher temperatures (Ortiz De Solorzano et al., 2016). The absorption spectrum showed in Fig. 2g evidenced that the NPs produced are suitable for the application in photodynamic therapy with high penetration depths because they show high absorbance in the NIR region of the electromagnetic spectrum.

Finally, organic–inorganic hybrid NPs were obtained by the electrostatic interaction between the positive charged polymeric NPs and the ultrasmall PVP stabilized inorganic CuS NPs to be subsequently applied in aPDT. Firstly, a study of the interaction between both NPs was carried out to obtain the maximum attachment of the CuS NPs onto the polymeric particles. For this, the modification of the Z-potential of the resulting hybrid particles was studied using different ratios of both materials (CuS NPs and polymeric NPs). After 1 h of interaction, it was observed in Figure S2a that, from a RS-PLGA-ICG:CuS NPs ratio of 1:0.5, the final hybrid vector reached a value of Z-potential of −15.7 ± 1.7 mV at pH 6 and, from this amount, the value of the zeta potential barely varied after increasing the CuS content. Thus, the optimum RS-PLGA-ICG:CuS NPs ratio was established at 1:0.5. It was also corroborated by the hydrodynamic diameter shown in Figure S2b where the agglomeration of the hybrid NPs was prevented from the ratio 1:0.1 and higher, due to charge stabilization.

Fig. 3 summarizes the physicochemical characterization of the optimum RS-PLGA-ICG@CuS NPs. Fig. 3a-b-d depict the scanning, transmission electron microscopy analysis and the colloidal solution of the resulting hybrid NPs that show a uniform particle size distribution measured from SEM images of 132 ± 47 nm (Fig. 3c). As it is depicted in Fig. 3f and S2b, the effective diameters of the resulting RS-PLGA-

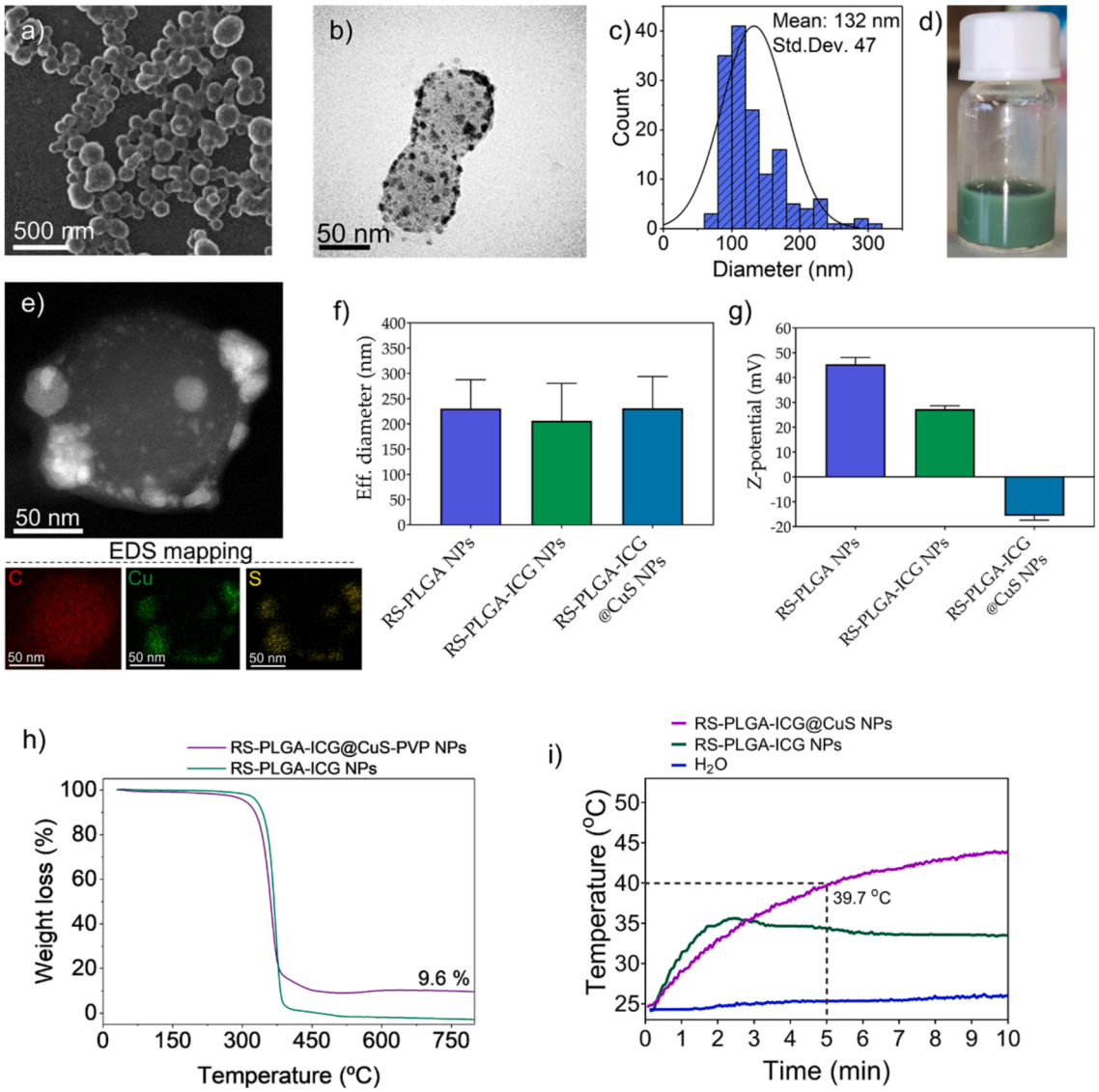

Fig. 3. a) Representative sem image of the RS-PLGA-ICG@CuS NPs, b) tem image of the RS-PLGA-ICG@CuS NPs, c) size distribution of RS-PLGA-ICG@CuS NPs obtained from the SEM measurements (N = 150), d) image of the RS-PLGA-ICG@CuS NPs colloidal suspension, e) representative HAADF-STEM image and EDS mapping of RS-PLGA-ICG@CuS NPs f) hydrodynamic diameter of RS-PLGA, RS-PLGA-ICG and RS-PLGA-ICG@CuS NPs, g) measurement of surface charge from Z-potential of RS-PLGA, RS-PLGA-ICG and RS-PLGA-ICG@CuS NPs at pH 6, h) thermogravimetric analysis of RS-PLGA-ICG (green line) and RS-PLGA-ICG@CuS NPs (purple line) and i) measurement of the heating rate of RS-PLGA-ICG (green line), RS-PLGA-ICG@CuS NPs (purple line) and water (blue line) under 808 nm, 1 W/cm^2 irradiation.

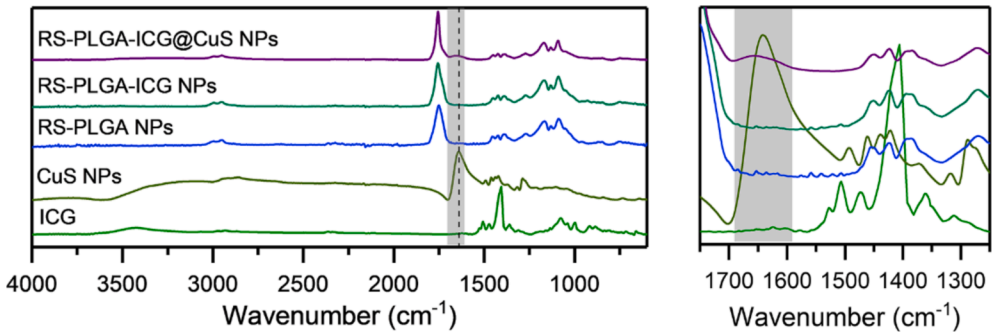

Fig. 4. FTIR spectra of pure ICG, CuS NPs, RS-PLGA, RS-PLGA-ICG and RS-PLGA-ICG@CuS NPs (left). Zoom in on the area where the differences were observed (right).

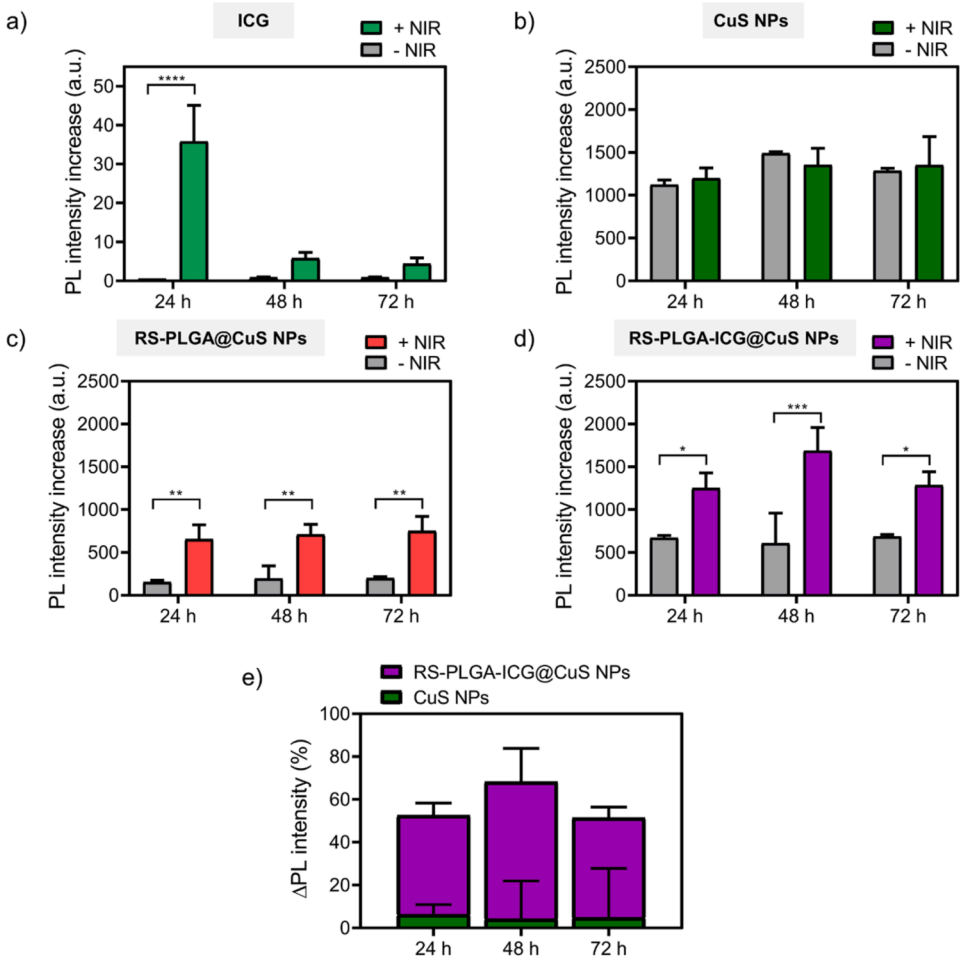

Fig. 5. Formation of reactive oxygen species (ROS) assessed by fluorescence using the DHR123 probe of: a) free ICG solution at a concentration of 100 ppm, b) CuS NPs, c) RS-PLGA@CuS NPs, d) RS-PLGA-ICG@CuS NPs and d) comparison of the increase in radical production between CuS NPs and RS-PLGA-ICG@CuS NPs. Data are represented as the mean ± SD of at least three independent measurements. Statistically significant differences between the non-irradiated samples and the irradiated ones (* $p < 0.05$; ** $p < 0.01$; *** $p < 0.001$; **** $p < 0.0001$) are also depicted.

ICG@CuS NPs that were determined by DLS, are smaller than the effective diameters measured by SEM imaging. This difference is generally rationalized because DLS provides the hydrodynamic diameter in a colloidal suspension, whereas SEM provides a physical diameter after drying the sample. The hydrodynamic particle sizes were similar when the polymeric NPs were produced with and without ICG (Fig. 3f) and with the CuS NPs decorating their surfaces, concluding that the ICG and CuS loads do not alter the final size of the photodynamic nanovector. The binding of the negatively charged CuS NPs at the shell of RS-PLGA-ICG NPs was also ratified by the Z-potential, resulting changes from positive values without presence of CuS NPs to negative values after the binding of CuS NPs on the polymers (Fig. 3g). CuS NPs were homogenously distributed on the shell of the RS-PLGA-ICG NPs as it is evidenced from the TEM and HAADF-STEM images, as well as from the EDS mapping (Fig. 3e). TGA analysis was designed to assess the fraction of organic and inorganic components and the CuS loading, obtaining that 9.6 wt.% of the hybrid nanovector was attributed to the presence of CuS (Fig. 3h). Finally, Fig. 3i depicts the photothermal properties of RS-PLGA-ICG NPs and RS-PLGA-ICG@CuS NPs. These properties were studied by monitoring the temperature of an aqueous dispersion of NPs (100 ppm) irradiated by a NIR laser (808 nm, 1 W/cm^2) and benchmarking it against the heating of water. After 5 min of NIR heating, the same time than in the antibacterial photodynamic experiments that will be commented afterwards, the temperature of the aqueous dispersion of RS-PLGA-ICG@CuS NPs increased only up to 39.7 °C from RT, achieving a temperature value slightly higher than that with RS-PLGA-ICG NPs due to the absorbance of CuS NPs (Ortiz De Solorzano et al., 2016).

FTIR spectroscopy was selected to evaluate the presence and the possible interactions between the polymers, ICG and CuS NPs. In Fig. 4, FTIR spectra are shown. All the polymeric NPs studied showed a strong vibration peak at 1755 cm^{-1}, owning to the carbonyl C = O stretching at 1762 cm^{-1} of the PLGA polymer(Prabhuraj et al., 2020) and C = O stretching at 1734 cm^{-1} of the RS polymer (Deshmukh and Naik, 2013). The ICG spectrum showed characteristic bands between 1400 and 1500 cm^{-1} due to aromatic C = C stretching and between 900 and 1100 cm^{-1} due to alkene C–H stretching (Lee et al., 2021). No peak related to ICG was observed in RS-PLGA-ICG or RS-PLGA-ICG@CuS NPs probably because of the low ICG loading (0.9 ± 0.1 wt.%) into the polymer NPs. On the other hand, spectra of CuS NPs showed peaks assigned mostly to PVP used as stabilizing molecule, such as the peak observed at 1640 cm^{-1} corresponding to the vibration of the C = O (Safo et al., 2019). Peaks observed at 1286 cm^{-1} can be attributed to the C = N stretching (Ramesan et al., 2018). The corresponding peak observed at 1640 cm^{-1} of the CuS NPs, highlighted in Fig. 4 as a shaded zone to favor its identification, can be slightly observed in the RS-PLGA-ICG@CuS NPs spectrum confirming the presence of CuS NPs into de polymeric ones, but it was not identified any feasible molecular interactions between the compounds.

The generation of ROS was assessed using the DHR123 probe. The samples exhibited no fluorescence signal in the absence of the DHR probe (Figure S3). Fig. 5a showed the production of ROS by an aqueous solution of free ICG. The measurement of ROS generation has

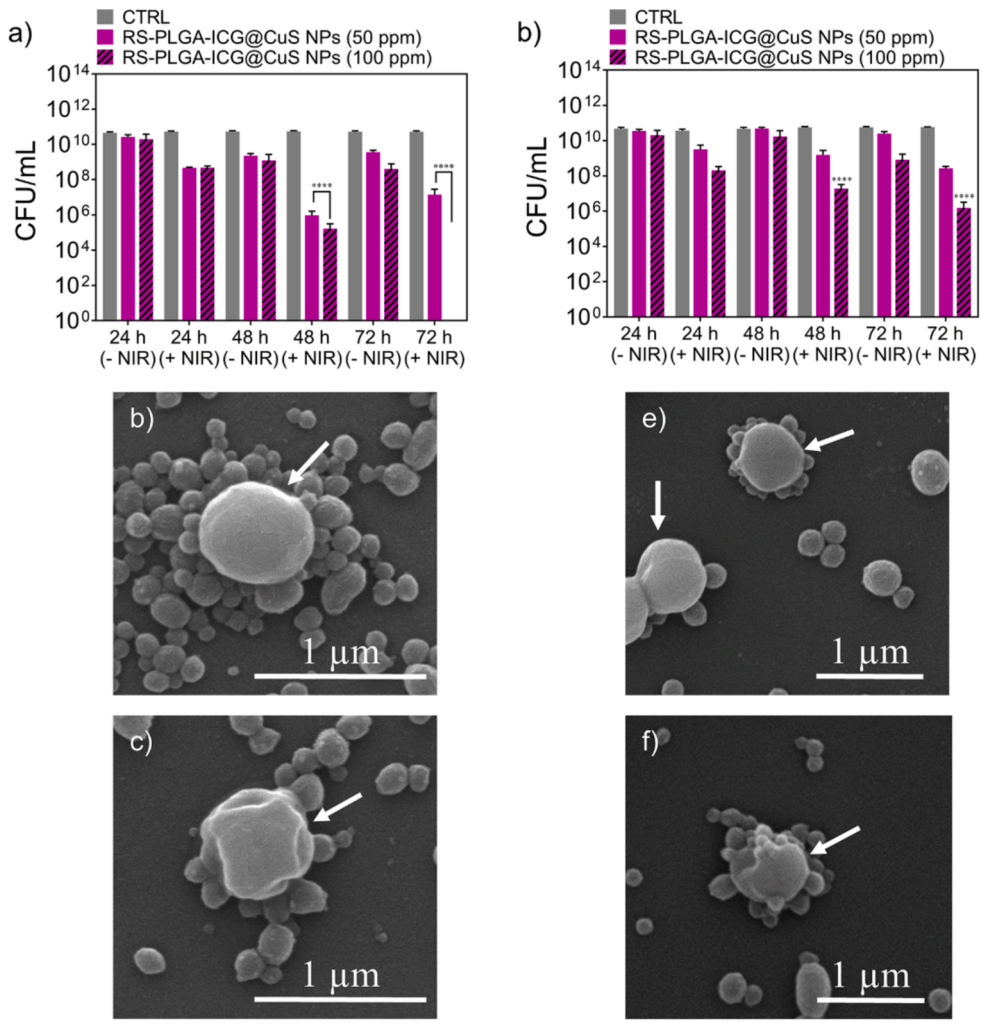

Fig. 6. Antibacterial photodynamic effect of RS-PLGA-ICG@CuS NPs treatment on: a) *S. aureus* b) SEM image of *S. aureus* before NIR treatment, c) SEM image of *S. aureus* after NIR treatment, d) USA300 MRSA, e) SEM image of USA300 MRSA before NIR treatment, f) SEM image of USA300 MRSA after NIR treatment. Bacteria are indicated with a white arrow. Data are represented as the mean ± SD of at least three independent measurements in duplicate. Statistically significant differences between the non-irradiated samples and the irradiated ones (****$p < 0.0001$) are also depicted.

demonstrated that ICG rapidly degrades under light exposure and over time, as previously mentioned, leading to a marked decrease in ROS production. This degradation compromises the therapeutic potential of ICG in PDT, highlighting the need of using stabilization strategies to enhance its photostability.

Our results indicate that both CuS NPs and RS-PLGA-ICG@CuS NPs produce similar levels of ROS under NIR irradiation after 5 min (Fig. 5b and 5d). However, the method of ROS production differs between the two types of particles, which could have significant implications for their use in PDT applications. CuS NPs were found to generate ROS even in absence of NIR irradiation, being rationalized by the presence of a copper ion-rich surface and sulfur vacancies (Mutalik et al., 2022) (Fig. 5b). The underlying mechanism could involve the intrinsic properties of CuS. CuS NPs can generate ROS due to their high redox activity and surface reactivity. In humid environments, CuS can be transformed to $CuSO_4$ and Cu^+ to Cu^{2+}, in presence of oxygen. Adsorbed water is hypothesized to act as a medium for this reaction, facilitating the surface dissolution of CuS into its respective ions and supplying protons to generate ROS via oxygen (Wu et al., 2020). Furthermore, CuS NPs exhibit multi-enzymatic capabilities, including catalase-like and peroxidase-like activities, which enhance ROS generation (Zhang et al., 2021),(Wang et al., 2023). Additionally, CuS NPs can participate in Fenton-like reactions, further promoting the conversion of hydrogen peroxide (H_2O_2) into hydroxyl radicals (•OH) (Raj and Jaiswal, 2021). These properties are particularly advantageous in applications requiring continuous ROS generation, such as certain antimicrobial treatments or cancer therapies where persistent oxidative stress is desired to induce cell damage or death.

In contrast, polymeric NPs exhibited a distinct pattern, where ROS generation significantly increased upon irradiation (Fig. 5c-d). This indicates that these NPs are activated by irradiation, specifically under NIR light, leading to enhanced ROS production. Consequently, in the absence of NIR irradiation, the polymeric NPs generated substantially fewer radicals. The ability to control ROS generation spatially and temporally with NIR light makes polymeric NPs highly suitable for targeted therapies. In PDT, precise control over ROS production minimizes damage to surrounding healthy tissues and enhances therapeutic efficacy.

The observed differences in ROS generation between CuS and hybrid NPs highlight their potential application in different therapeutic scenarios. Hybrid NPs showed the capability to generate 60–80 % more ROS upon irradiation. In contrast, the difference in ROS generation between CuS NPs with and without laser exposure was not more than 7 % (Fig. 5e).

In order to prevent a photothermal activity and to ensure the antibacterial activity was caused by only a photodynamic action, a time of

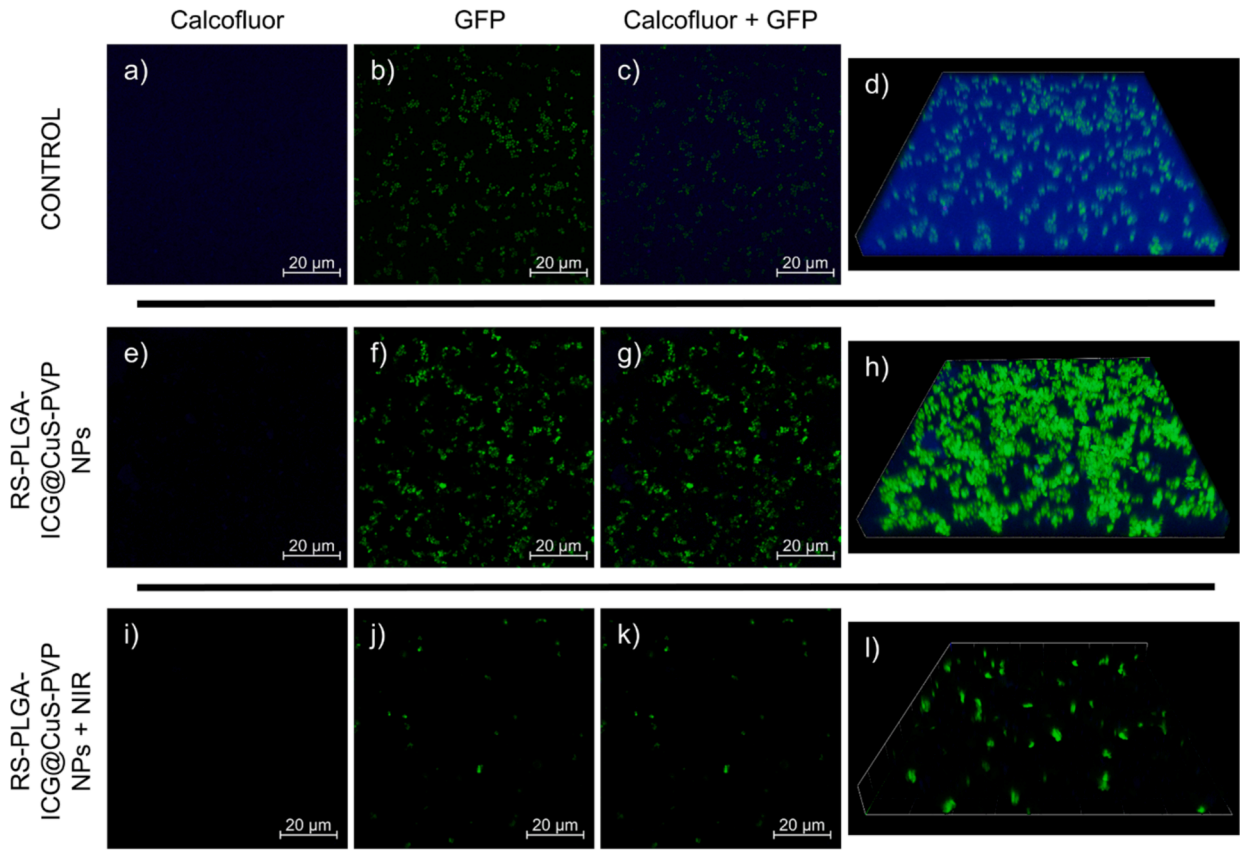

Fig. 7. Confocal microscopy images of biofilms of *S. aureus*-GFP stained with calcofluor. a-d) *S. aureus*-GFP biofilm without treatment (control), e-h) *S. aureus*-GFP biofilm after RS-PLGA-ICG@CuS NPs treatment for 24 h and i-l) *S. aureus*-GFP with RS-PLGA-ICG@CuS NPs and NIR irradiation (808 nm, 1 W/cm^2, 5 min). Blue fluorescence, corresponding to the calcofluor staining, shows the biofilm extracellular matrix and the GFP fluorescent protein shows the viable *S. aureus* bacteria as green dots.

irradiation of 5 min was selected. At this time of irradiation (808 nm and 1 W/cm^2), the temperature reached was below 40 °C as can be seen in Fig. 3i. In this manner, the approach mitigates the risk of thermal injury to the patient's skin, minimizing the adverse effects associated with thermal exposure. Previous works have demonstrated that this temperature is not enough to produce any viability reduction in the bacterial cell growth (Wang et al., 2017),(Garin et al., 2021). Additionally, three short irradiations of 5 min every 24 h were chosen to minimize light exposure time. It was expected that the encapsulated ICG would gradually be released every 24 h from the polymeric NPs to be available and increase its antimicrobial potential after each irradiation.

To investigate the antibacterial activity of the hybrid NPs, two *S. aureus* strains, *S. aureus* ATCC 25923 (*S. aureus*) and USA300 MRSA, were selected to perform the microbiological assays. After been incubated the bacteria cultures (for 24, 48 and 72 h) with free ICG, RS-PLGA NPs, RS-PLGA@CuS NPs, RS-PLGA-ICG NPs and RS-PLGA-ICG@CuS NPs, the serial dilution method was carried out with and without NIR pulses (5 min of 808 nm laser irradiation at 1 W/cm^2) at each time interval. Controls without treatment but only NIR irradiation were performed to assure that the irradiation conditions selected did not reduce cell viability by themselves (control samples). RS-PLGA NPs were no cytotoxic for both *S. aureus* and USA300 MRSA (Figure S4).

When *S. aureus* was incubated with free ICG (Figure S5a) and first irradiated (24 h), a 3-log reduction was observed for both concentrations assayed (50 and 100 ppm). But, after the second irradiation (48 h), only the highest concentration was capable to maintain the viability reduction although the antibacterial efficacy was not increased, maintaining the 3-log reduction. At 72 h, bacteria were re-grown again until reaching their stationary phase, probably due to the ICG degradation along time (Fig. 1e). For the USA300 MRSA treatment, a 2-log reduction was observed after the first irradiation (24 h) but, after 48 and 72 h irradiation, bacteria recovered their initial burden (FigureS5b). No significant viability reduction was observed without irradiation for both bacterial strains. Currently, no relationship between resistance and response to photodynamic therapy has been reported but, according to our results, different bacterial strains may respond differently to this photodynamic therapy due to structural differences in their cell walls (Topaloglu et al., 2013). The antibacterial activity of the encapsulated ICG was lower than that of the free form ICG. Figure S6 depicts the absence of viability reduction for the RS-PLGA-ICG NPs without irradiation for both *S. aureus* and USA300 MRSA. As could be observed in Figure S6a for *S. aureus*, RS-PLGA-ICG NPs are capable to reduce 2–log for an ICG encapsulated concentration of 100 ppm and only 1-log for 50 ppm when they are irradiated for the first time (24 h). After that time point, the bacteria viability seems to recover until reaching the initial bacterial concentration. For the USA300 MRSA (Figure S6b), only 1-log reduction is observed for the first irradiation (24 h) without noticing any antibacterial effect in the rest of the irradiations. As expected, the activity of the encapsulated ICG is decreased due to a slow and prolonged release over time in addition to the degradation of the free photosensitizer. At this point, it could be concluded that encapsulation prevents the ICG from degradation but reduces its bioavailability.

Figure S7 showed the behavior of bacteria when they were incubated with RS-PLGA@CuS NPs. A slight decrease in survival rate was observed over time with and without NIR irradiation. This surely is due to the toxicity generated by copper when leached in addition to the reactive oxygen species generated (Giachino and Waldron, 2020). After 72 h of incubation, for both bacteria *S. aureus* and USA300 MRSA, the difference in viability of the 3-times irradiated bacteria and those not irradiated is 1-log reduction apart. So apparently, the toxic activity of copper is being

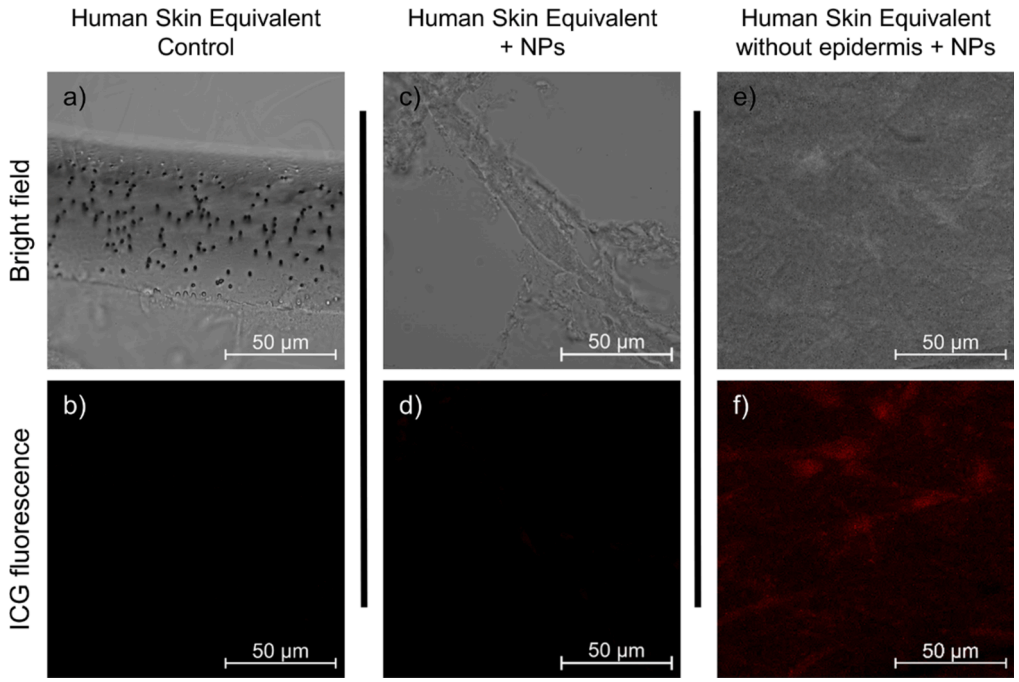

Fig. 8. a) Bright field image of a control human skin equivalent, b) confocal fluorescence image of a control skin equivalent, c) bright field image of a human skin equivalent treated with RS-PLGA-ICG@CuS NPs, d) confocal fluorescence image of a human skin equivalent treated with RS-PLGA-ICG@CuS NPs, e) bright field image of a human skin equivalent without epidermis treated with RS-PLGA-ICG@CuS NPs and f) confocal fluorescence image of a human skin equivalent without epidermis treated with RS-PLGA-ICG@CuS NPs. All the samples observed correspond to sections of the lower zone of the epidermis. The red fluorescence observed indicates the presence of RS-PLGA-ICG@CuS NPs.

more pronounced than the radicals generated by NIR irradiation.

The hybrid RS-PLGA-ICG@CuS NPs yielded a potentiated effect due to the synergetic photodynamic activity of ICG and CuS, as previously reported when they were added without being supported in a polymeric vector (Garin et al., 2021). After the first NIR pulse (24 h), the survival rate was already reduced more than 90 % for both *S. aureus* and USA300 MRSA. Notably, the equivalent concentration of 100 ppm of ICG, managed to kill the entire *S. aureus* population after three NIR pulses (72 h) (Fig. 6a) and the 99.99 % of USA300 MRSA (Fig. 6d). In addition, one of the potential mechanisms of antimicrobial action of the final hybrid NPs was examined by SEM visualization. In Fig. 6b and 6e *S. aureus* and USA300 MRSA bacteria are shown after RS-PLGA-ICG@CuS NPs treatment without NIR pulses. A rounded morphology can be observed in contact with the hybrid NPs surrounding the bacteria without any cell wall damage. After the NIR pulses and consequent antimicrobial therapy (Fig. 6c-f), both strains showed a wrinkled and damaged cellular peptidoglycan-based wall, which means cell membrane damage due to the action of ROS (Song et al., 2019)'(Xiang et al., 2019).

As we mentioned before, biofilm formation in wound infections is one of the most difficult-to-treat complications that hinder wound healing. Biofilms are robust structures which confer antibiotic resistance to bacteria because of several reasons, including low penetration of the antibiotics through the extracellular matrix formed by extracellular polymeric substances (EPS) of the biofilm or slowed growth that reduces the effectiveness of antibiotics that target binary fission, among others (Dincer et al., 2020). Several studies have demonstrated that aPDT is one of the current promising strategies for biofilm treatment by producing cell lysis by ROS production, being possible in this case the irradiation of a determined infected area making the treatment highly spatially specific (Hu et al., 2018). In this work, confocal microscopy was selected to observe the antibiofilm action in a qualitative manner. GFP-expressing antibiotic-sensitive *S. aureus* (MSSA) was selected to be able to observe the alive bacteria (green spots) and calcofluor white stain was used to monitor biofilm formation (stained in blue). By studying the fluorescence of the calcofluor, morphological and structural changes in the biofilm can be highlighted, while the fluorescence emitted by the GFP provides information on the qualitative reduction of viable bacteria attached to the substrate as part of the biofilm. As can be seen in Fig. 7d, alive bacteria used as control were able to grow and form a layer of biofilm when they were not treated with the hybrid polymeric NPs nor irradiated. However, when a preformed biofilm was incubated for 24 h at 37 °C with RS-PLGA-ICG@CuS NPs (100 ppm corresponding to ICG load) in the absence of NIR light, the amount of calcofluor staining was drastically reduced, observing mostly alive bacteria stained in green but no biofilm formation (Fig. 7h). These results suggest that the hybrid NPs produce some antibiofilm effect although they are not capable to effectively kill bacteria. It is reported that ionic copper is capable to interact with the EPS of the biofilm and interferes with biofilm formation (Gomes et al., 2020),(Colin et al., 2021). Baker et al. (Baker et al., 2010) demonstrated in their study the stress response when *S. aureus* is exposed to high copper levels. In their investigation they identified a plenty of adaptation mechanisms to this copper stress, and one of these mechanisms was related to the regulation of virulence factors in the bacteria, such as biofilm formation. They were able to identify a repression of the expression of gene regulators of the biofilm formation, as the genes *agr* and *sae*, among others. When biofilm was treated with RS-PLGA-ICG@CuS NPs + NIR irradiation (Fig. 7i-l) it was observed that the biofilm disappeared completely and a highly marked reduction in viable bacteria was also observed. Therefore, the qualitative results shown in Fig. 7, demonstrate that the combination of the hybrid vector and NIR irradiation was highly effective against preformed mature biofilm, being able to destroy it and kill almost all the bacteria that formed it.

Although the NPs showed toxicity towards cell lines (human dermal fibroblasts and human keratinocytes, data not shown) in 2D cell cytotoxicity studies at the antibacterial concentrations, the therapeutic benefit observed was considered of significant relevance, being comparable to an antiseptic action. In this case, due to the effective antibacterial action achieved after light exposure, the effect of cell toxicity

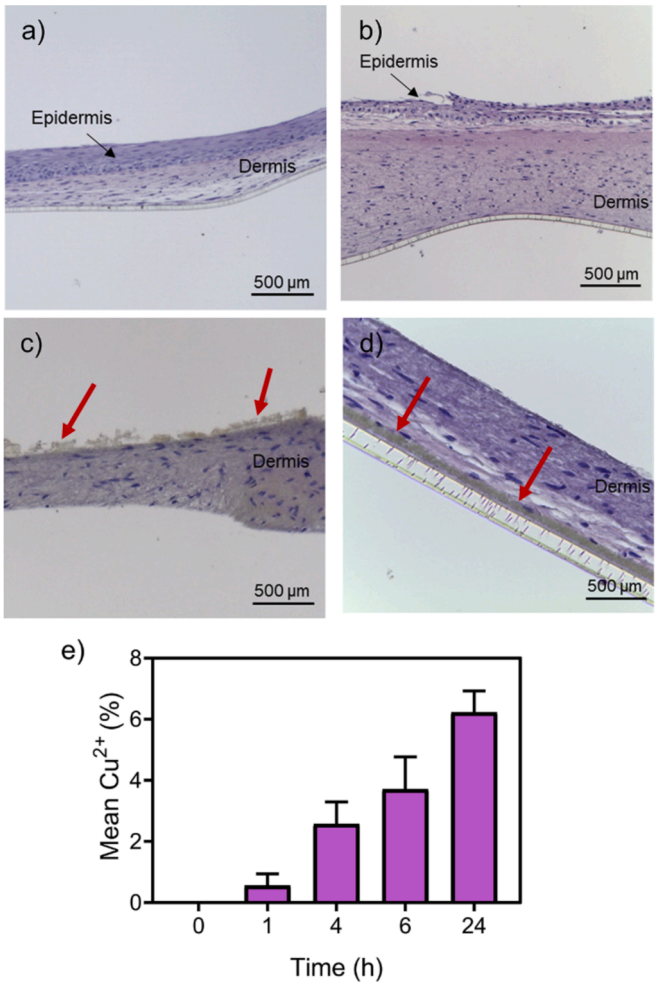

Fig. 9. Histology images of human *in vitro* skin equivalents of treated with RS-PLGA-ICG@CuS NPs. In a) no treated control skin, b) treated skin with epidermis, c) treated skin without epidermis with NPs at the surface, and d) treated skin without epidermis with NPs in the lower dermis. Red arrows point to the RS-PLGA-ICG@CuS NP aggregates at different locations of the *in vitro* skin equivalents. In e) copper permeability at different timepoints of *in vitro* skin equivalents without epidermis treated with RS-PLGA-ICG@CuS NPs.

was considered negligible because the pathogenic bacteria were eliminated. In potential real scenario new regenerative stem cells would migrate and regenerate the wound now free of pathogenic bacteria. In addition, it is important to note that the conditions in the 2D study may not fully reflect the complex interactions in a physiological environment. In contrast, in the 3D study with human cell-derived artificial skin models, which we believe provides a more realistic approximation to the clinical scenario, histological analysis showed no signs of cytoxicity, as illustrated in Fig. 9. This 3D approach therefore offers a more accurate and promising basis for evaluating the therapeutic potential of these NPs for future topical applications because it better mimics the physiological environment and spatial configuration of human cells.

To explore the performance of RS-PLGA-ICG@CuS NPs in a potential wound bed, plasma-derived dermo-epidermal equivalents in early maturation stages were used as a human skin model. After 15 days in culture, with the help of a precision clamp, the epidermis of the skin equivalents was carefully removed to expose the dermis and create the wound bed. Skin equivalents with the epidermis were also used as control. After 24 h in culture, no fluorescence was observed in the dermal fraction of the skin without NPs treatment, demonstrating that the skin does not exhibit autofluorescence (Fig. 8a-b). In skin constructs with epidermis (Fig. 8c-d), fluorescence images revealed no presence of RS-PLGA-ICG@CuS NPs in the dermal fraction. Conversely, in skin constructs without epidermis (Fig. 8e-f) the images revealed the presence of NPs, as they appeared to have successfully penetrated the dermis.

Moreover, structural analysis of the skin equivalents using H&E staining, showed a correct epidermal differentiation of the construct before the differentiation process (Fig. 9a) and 24 h after treatment (Fig. 9b). Conversely, in the wound bed (skin equivalents without epidermis) the RS-PLGA-ICG@CuS NP agglomerates can be visualized as dark brown spots either on the surface (Fig. 9c, red arrows) or in the reticular dermis (Fig. 9d, red arrows), proving their ability to distribute all over the area of the wound. This fact is further confirmed by the permeation analysis, which shows a proportional increase in the percentage of Cu^{2+} ions present over time, derived from the initially added NPs, which is an indication of the percolation ability of the hybrid NPs (Fig. 9e).

While early maturation stages of the skin construct are required to mimic the wound bed, the presented data prove the epidermal barrier function fidelity of the skin equivalents. This confirms the potential of plasma-derived fibrin skin models as a physiologically relevant and reliable *in vitro* system to test the performance of dermal treatments.

4. Conclusions

Herein we report how hybrid biodegradable polymeric nanoparticles containing ICG and CuS are able to elicit a strong antimicrobial photodynamic-based action on pathogenic bacteria. A synergetic action is responsible for a total bacterial eradication over wild type *S. aureus* and a 99.99 % reduction in the viability of MRSA after only 3 successive short cycles (5 min) of NIR light irradiation. In addition, those nanoparticles are able to strongly reduce the biomass of mature biofilms. The biodegradable nature of the composing organic materials (i.e., PLGA, ICG and PVP) together with the demonstrated degradation under physiological conditions of the CuS NPs nanoparticles used highlight the clear advantage of this hybrid photosensitizer on the prevention of potentially cytotoxic components bioaccumulation. A human skin substitute was also used to analyze the permeation characteristics of the hybrid nanoparticles in the presence or absence of the epidermal layer. Quantitative ionic copper analysis and qualitative ICG fluorescence measurements revealed that the nanoparticles were unable to cross the epidermis but they were able to permeate through a dermal layer lacking epidermis, which make them interesting for their potential application in the elimination of pathogenic bacteria from topical wounds.

CRediT authorship contribution statement

Cristina Yus: Writing – review & editing, Writing – original draft, Validation, Methodology, Investigation, Formal analysis, Data curation. **Teresa Alejo:** Writing – review & editing, Methodology, Investigation, Formal analysis, Data curation. **Cristina Quílez:** Writing – review & editing, Writing – original draft, Validation, Methodology, Investigation, Formal analysis, Data curation. **Silvia Irusta:** Writing – review & editing, Validation, Supervision, Investigation, Formal analysis. **Diego Velasco:** Writing – review & editing, Validation, Supervision, Investigation, Funding acquisition, Formal analysis. **Manuel Arruebo:** Writing – review & editing, Writing – original draft, Validation, Supervision, Investigation, Funding acquisition, Formal analysis, Conceptualization. **Victor Sebastian:** Writing – review & editing, Writing – original draft, Validation, Supervision, Investigation, Funding acquisition, Formal analysis, Conceptualization.

Declaration of competing interest

The authors declare that they have no known competing financial interests or personal relationships that could have appeared to influence

the work reported in this paper.

Acknowledgments

This research was funded by the Spanish Ministry of Science and Innovation (grants numbers PID2021-127847OB-I00 and PID2020-113987RB-I00). We also acknowledge the financial support of MCIN/AEI/10.13039/501100011033 and the NextGenerationEU/PRTR thanks to the projects PDC2022-133866-I00 and PDC2021-121405-I00. CIBER-BBN is an initiative funded by the VI National R&D&i Plan 2008-2011, Iniciativa Ingenio 2010, Consolider Program, CIBER Actions and financed by the Instituto de Salud Carlos III (Spain) with assistance from the Fondo Europeo de Desarrollo Regional (Feder). NANBIOSIS and LMA- ELECMI ICTS (University of Zaragoza, Spain) are also acknowledged. Authors would like to acknowledge the use of Servicios Científico Técnicos del CIBA (IACS-Universidad de Zaragoza).

Appendix A. Supplementary data

Supplementary data to this article can be found online at https://doi.org/10.1016/j.ijpharm.2024.124951.

Data availability

Data will be made available on request.

References

Alves, E., Faustino, M.A.F., Neves, M.G., Cunha, A., Tome, J., Almeida, A., 2014. An insight on bacterial cellular targets of photodynamic inactivation. Future Med. Chem. 6, 141–164. https://doi.org/10.4155/fmc.13.211.

Baker, J., Sitthisak, S., Sengupta, M., Johnson, M., Jayaswal, R.K., Morrissey, J.A., 2010. Copper Stress Induces a Global Stress Response in Staphylococcus aureus and Represses sae and agr Expression and Biofilm Formation. Appl. Environ. Microbiol. 76, 150–160. https://doi.org/10.1128/AEM.02268-09.

Carretero, M., Guerrero-Aspizua, S., Illera, N., Galvez, V., Navarro, M., García-García, F., Dopazo, J., Jorcano, J.L., Larcher, F., del Rio, M., 2016. Differential Features between Chronic Skin Inflammatory Diseases Revealed in Skin-Humanized Psoriasis and Atopic Dermatitis Mouse Models. J. Invest. Dermatol. 136, 136–145. https://doi.org/10.1038/JID.2015.362.

Cieplik, F., Deng, D., Crielaard, W., Buchalla, W., Hellwig, E., Al-Ahmad, A., Maisch, T., 2018. Antimicrobial photodynamic therapy – what we know and what we don't. Crit. Rev. Microbiol. 44, 571–589. https://doi.org/10.1080/1040841X.2018.1467876.

Colin, M., Carré, G., Klingelschmitt, F., Reffuveille, F., Gangloff, S.C., 2021. Copper alloys to prevent bacterial biofilm formation on touch surfaces. Mater. Lett. 305, 1–4. https://doi.org/10.1016/j.matlet.2021.130712.

Cubo, N., Garcia, M., Del Cañizo, J.F., Velasco, D., Jorcano, J.L., 2016. 3D bioprinting of functional human skin: production and in vivo analysis. Biofabrication 9, 15006. https://doi.org/10.1088/1758-5090/9/1/015006.

Deshmukh, R.K., Naik, J.B., 2013. Diclofenac Sodium-Loaded Eudragit® Microspheres: Optimization Using Statistical Experimental Design. J. Pharm. Innov. 8, 276–287. https://doi.org/10.1007/s12247-013-9167-9.

Dillen, K., Vandervoort, J., Van den Mooter, G., Ludwig, A., 2006. Evaluation of ciprofloxacin-loaded Eudragit® RS100 or RL100/PLGA nanoparticles. Int. J. Pharm. 314, 72–82. https://doi.org/10.1016/j.ijpharm.2006.01.041.

Dincer, S., Uslu, F.M., Delik, A., 2020. Antibiotic Resistance in Biofilm, in. Bacterial Biofilms. Intechopen. https://doi.org/10.5772/intechopen.92388.

Garapati, C., Boddu, S.H.S., Jacob, S., Ranch, K.M., Patel, C., Babu, R.J., Tiwari, A.K., Yasin, H., 2023. Photodynamic therapy: a special emphasis on nanocarrier-mediated delivery of photosensitizers in antimicrobial therapy. Arab. J. Chem. 16, 104583.

Garin, C., Alejo, T., Perez-Laguna, V., Prieto, M., Mendoza, G., Arruebo, M., Sebastian, V., Rezusta, A., 2021. Chalcogenide nanoparticles and organic photosensitizers for synergetic antimicrobial photodynamic therapy. J. Mater. Chem. B 9, 6246–6259. https://doi.org/10.1039/d1tb00972a.

Ghorbani, J., Rahban, D., Aghamiri, S., Teymouri, A., Bahador, A., 2018. Photosensitizers in antibacterial photodynamic therapy: an overview. Laser Ther. 27, 293–302. https://doi.org/10.5978/islsm.27_18-RA-01.

Giachino, A., Waldron, K.J., 2020. Copper tolerance in bacteria requires the activation of multiple accessory pathways. Mol. Microbiol. 114, 377–390. https://doi.org/10.1111/mmi.14522.

Gomes, I.B., Simões, M., Simões, L.C., 2020. Copper surfaces in biofilm control. Nanomaterials 10, 1–21. https://doi.org/10.3390/nano10122491.

Gómez, C., Galán, J.M., Torrero, V., Ferreiro, I., Pérez, D., Palao, R., Martínez, E., Llames, S., Meana, A., Holguín, P., 2011. Use of an autologous bioengineered composite skin in extensive burns: Clinical and functional outcomes. A Multicentric Study. Burns 37, 580–589. https://doi.org/10.1016/j.burns.2010.10.005.

Guerrero-Aspizua, S., García, M., Murillas, R., Retamosa, L., Illera, N., Duarte, B., Holguín, A., Puig, S., Hernández, M.I., Meana, A., Jorcano, J.L., Larcher, F., Carretero, M., Del Río, M., 2010. Development of a bioengineered skin-humanized mouse model for psoriasis: dissecting epidermal-lymphocyte interacting pathways. Am. J. Pathol. 177, 3112–3124. https://doi.org/10.2353/ajpath.2010.100078.

Hoffart, V., Ubrich, N., Simonin, C., Babak, V., Vigneron, C., Hoffman, M., Lecompte, T., Maincent, P., 2002. Low molecular weight heparin- loaded polymeric nanoparticles : formulation, characterization, and release characteristics. Drug Dev. Ind. Pharm. 28, 1091–1099. https://doi.org/10.1081/DDC-120014576.

Hu, X., Huang, Y.Y., Wang, Y., Wang, X., Hamblin, M.R., 2018. Antimicrobial photodynamic therapy to control clinically relevant biofilm infections. Front. Microbiol. 9, 1–24. https://doi.org/10.3389/fmicb.2018.01299.

James, W.D., Elston, D.M., Treat, J.R., Rosenbach, M.A., 2019. Andrews' diseases of the skin: Clinical dermatology. J. Am. Acad. Dermatol. 81, 1–11. https://doi.org/10.1016/j.jaad.2019.08.041.

Kolarsick, P., Kolarsick, M.A., Goodwin, C., 2011. Anatomy and Physiology of the Skin. J. Dermatol. Nurses. Assoc. 3, 203–213. https://doi.org/10.1097/JDN.0b013e3182274a98.

Lafuente, B., Downs, R.T., Yang, H., Stone, N., 2016. The power of databases: the RRUFF project. Highlights in Mineralogical Crystallography. 1–30.

Lee, E.H., Lee, M.K., Lim, S.J., 2021. Enhanced stability of indocyanine green by encapsulation in zein-phosphatidylcholine hybrid nanoparticles for use in the phototherapy of cancer. Pharmaceutics 13, 1–10. https://doi.org/10.3390/pharmaceutics13030305.

Li, L., Rashidi, L.H., Yao, M., Ma, L., Chen, L., Zhang, J., Zhang, Y., Chen, W., 2017. CuS nanoagents for photodynamic and photothermal therapies: Phenomena and possible mechanisms. Photodiagnosis Photodyn. Ther. 19, 5.

Liu, X., Ren, Q., Fu, F., Zou, R., Wang, Q., Xin, G., Xiao, Z., Huang, X., Liu, Q., Hu, J., 2015. CuS@mSiO2-PEG core-shell nanoparticles as a NIR light responsive drug delivery nanoplatform for efficient chemo-photothermal therapy. Dalt. Trans. 44, 10343–10351. https://doi.org/10.1039/c5dt00198f.

Llames, S.G., Del Rio, M., Larcher, F., García, E., García, M., Escamez, M.J., Jorcano, J.L., Holguín, P., Meana, A., 2004. Human plasma as a dermal scaffold for the generation of a completely autologous bioengineered skin. Transplantation 77, 350–355. https://doi.org/10.1097/01.TP.0000112381.80964.85.

Llames, S., García, E., García, V., del Río, M., Larcher, F., Jorcano, J.L., López, E., Holguín, P., Miralles, F., Otero, J., Meana, A., 2006. Clinical results of an autologous engineered skin. Cell Tissue Bank. 7, 47–53. https://doi.org/10.1007/s10561-004-7253-4.

Ma, Y., Sadoqi, M., Shao, J., 2012. Biodistribution of indocyanine green-loaded nanoparticles with surface modifications of PEG and folic acid. Int. J. Pharm. 436, 25–31. https://doi.org/10.1016/j.ijpharm.2012.06.007.

Magadla, A., Oluwole, D.O., Managa, M., Nyokong, T., 2019. Physicochemical and antimicrobial photodynamic chemotherapy (against E. coli) by indium phthalocyanines in the presence of silver–iron bimetallic nanoparticles. Polyhedron 162, 30–38. https://doi.org/10.1016/j.poly.2019.01.032.

Maisch, T., 2015. Resistance in antimicrobial photodynamic inactivation of bacteria. Photochem. Photobiol. Sci. 14, 1518–1526. https://doi.org/10.1039/c5 pp00037h.

Makadia, H.K., Siegel, S.J., 2011. Poly Lactic-co-Glycolic Acid (PLGA) as Biodegradable Controlled Drug Delivery Carrier. Polymers (basel). 3, 1377–1397. https://doi.org/10.3390/polym3031377.

Martínez-Santamaría, L., Conti, C.J., Llames, S., García, E., Retamosa, L., Holguín, A., Illera, N., Duarte, B., Camblor, L., Llaneza, J.M., Jorcano, J.L., Larcher, F., Meana, Á., Escámez, M.J., Del Río, M., 2013. The regenerative potential of fibroblasts in a new diabetes-induced delayed humanised wound healing model. Exp. Dermatol. 22, 195–201. https://doi.org/10.1111/exd.12097.

Mazlyzam, A.L., Aminuddin, B.S., Fuzina, N.H., Norhayati, M.M., Fauziah, O., Isa, M.R., Saim, L., Ruszymah, B.H.I., 2007. Reconstruction of living bilayer human skin equivalent utilizing human fibrin as a scaffold. Burns 33, 355–363. https://doi.org/10.1016/j.burns.2006.08.022.

Mendoza, G., Regiel-Futyra, A., Andreu, V., Sebastián, V., Kyzioł, A., Stochel, G., Arruebo, M., 2017. Bactericidal Effect of Gold-Chitosan Nanocomposites in Coculture Models of Pathogenic Bacteria and Human Macrophages. ACS Appl. Mater. Interfaces 9, 17693–17701. https://doi.org/10.1021/acsami.6b15123.

Mohammadi, G., Namadi, E., Mikaeili, A., Mohammadi, P., Adibkia, K., 2017. Preparation and physicochemical characterization of the nystatin-loaded Eudragit RS100/PLGA nanoparticles and evaluation of their anti-fungal properties against Candida albicans. J. Drug Deliv. Sci. Technol. 38, 90–96. https://doi.org/10.1016/j.jddst.2017.02.004.

Montero, A., Quílez, C., Valencia, L., Girón, P., Jorcano, J.L., Velasco, D., 2021. Effect of fibrin concentration on the in vitro production of dermo-epidermal equivalents. Int. J. Mol. Sci. 22. https://doi.org/10.3390/ijms22136746.

Mutalik, C., Okoro, G., Krisnawati, D.I., Jazidie, A., Rahmawati, E.Q., Rahayu, D., Hsu, W.-T., Kuo, T.-R., 2022. Copper sulfide with morphology-dependent photodynamic and photothermal antibacterial activities. J. Colloid Interface Sci. 607, 1825–1835.

Ortiz De Solorzano, I., Prieto, M., Mendoza, G., Alejo, T., Irusta, S., Sebastian, V., Arruebo, M., 2016. Microfluidic Synthesis and Biological Evaluation of Photothermal Biodegradable Copper Sulfide Nanoparticles. ACS Appl. Mater. Interfaces 8, 21545–21554. https://doi.org/10.1021/acsami.6b05727.

Paesa, M., Remirez, C., Ganuza, D., Alejo, T., Yus, C., Irusta, S., Arruebo, M., Sebastian, V., Mendoza, G., 2023. Journal of Colloid and Interface Science Elucidating the mechanisms of action of antibiotic-like ionic gold and biogenic gold nanoparticles against bacteria. J. Colloid Interface Sci. 633, 786–799. https://doi.org/10.1016/j.jcis.2022.11.138.

Piksa, M., Lian, C., Samuel, I.C., Pawlik, K.J., Samuel, I.D.W., Matczyszyn, K., 2023. Chem Soc Rev The role of the light source in antimicrobial photodynamic therapy. Chem. SO 52, 1697–1722. https://doi.org/10.1039/d0cs01051k.

Prabhuraj, R.S., Bomb, K., Srivastava, R., Bandyopadhyaya, R., 2020. Selection of superior targeting ligands using PEGylated PLGA nanoparticles for delivery of curcumin in the treatment of triple-negative breast cancer cells. J. Drug Deliv. Sci. Technol. 57, 101722. https://doi.org/10.1016/j.jddst.2020.101722.

Proksch, E., Brandner, J.M., Jensen, J.-M., 2008. The skin: an indispensable barrier. Exp. Dermatol. 17, 1063–1072. https://doi.org/10.1111/j.1600-0625.2008.00786.x.

Quílez, C., Valencia, L., González-Rico, J., Suárez-Cabrera, L., Amigo-Morán, L., Jorcano, J.L., Velasco, D., 2024. In vitro induction of hair follicle signatures using human dermal papilla cells encapsulated in fibrin microgels. Cell Prolif. 57, e13528. https://doi.org/10.1111/cpr.13528.

Rahman, K.M.M., Giram, P., Foster, B.A., You, Y., 2023. Photodynamic Therapy for Bladder Cancers, A Focused Review†. Photochem. Photobiol. 99, 420–436.

Raj, S.I., Jaiswal, A., 2021. Nanoscale transformation in CuS Fenton-like catalyst for highly selective and enhanced dye degradation. J. Photochem. Photobiol. A Chem. 410, 113158. https://doi.org/10.1016/j.jphotochem.2021.113158.

Ramesan, M.T., Jayakrishnan, P., Anilkumar, T., Mathew, G., 2018. Influence of copper sulphide nanoparticles on the structural, mechanical and dielectric properties of poly (vinyl alcohol)/poly(vinyl pyrrolidone) blend nanocomposites. J. Mater. Sci. Mater. Electron. 29, 1992–2000. https://doi.org/10.1007/s10854-017-8110-0.

Randall, M.J., Jüngel, A., Rimann, M., Wuertz-Kozak, K., 2018. Advances in the Biofabrication of 3D Skin in vitro: Healthy and Pathological Models. Front. Bioeng. Biotechnol. 6, 154. https://doi.org/10.3389/fbioe.2018.00154.

Safo, I.A., Werheid, M., Dosche, C., Oezaslan, M., 2019. Nanoscale Advances The role of polyvinylpyrrolidone (PVP) as a capping and structure-directing agent in the formation of Pt nanocubes. Nanoscale Adv. 1, 3095–3106. https://doi.org/10.1039/c9na00186g.

Saxena, V., Sadoqi, M., Shao, J., 2003. Degradation Kinetics of Indocyanine Green in Aqueous Solution. J. Pharm. Sci. 92, 2090–2097. https://doi.org/10.1081/DDC-120025459.

Saxena, V., Sadoqi, M., Shao, J., 2004. Indocyanine green-loaded biodegradable nanoparticles: preparation, physicochemical characterization and in vitro release. Int. J. Pharm. 278, 293–301. https://doi.org/10.1016/j.ijpharm.2004.03.032.

Shan, W., Chen, R., Zhang, Q., Zhao, J., Chen, B., Zhou, X., Ye, S., Bi, S., Nie, L., Ren, L., 2018. Improved Stable Indocyanine Green (ICG)-Mediated Cancer Optotheranostics with Naturalized Hepatitis B Core Particles. Adv. Mater. 30, 1–11. https://doi.org/10.1002/adma.201707567.

Shirata, C., Kaneko, J., Inagaki, Y., Kokudo, T., Sato, M., Kiritani, S., Akamatsu, N., Arita, J., Sakamoto, Y., Hasegawa, K., Kokudo, N., 2017. Near-infrared photothermal/photodynamic therapy with indocyanine green induces apoptosis of hepatocellular carcinoma cells through oxidative stress. Sci. Rep. 7, 13958. https://doi.org/10.1038/s41598-017-14401-0.

Sipahi, O.R., 2008. Economics of antibiotic resistance. Expert Rev. Anti. Infect. Ther. 6, 523–539. https://doi.org/10.1586/14787210.6.4.523.

Song, Z., Wu, Y., Wang, H., Han, H., 2019. Synergistic antibacterial effects of curcumin modified silver nanoparticles through ROS-mediated pathways. Mater. Sci. Eng. C 99, 255–263. https://doi.org/10.1016/j.msec.2018.12.053.

Thapa, S.P., Shrestha, S., Anal, A.K., 2020. Addressing the antibiotic resistance and improving the food safety in food supply chain (farm-to-fork) in Southeast Asia. Food Control 108, 106809. https://doi.org/10.1016/j.foodcont.2019.106809.

Topaloglu, N., Gulsoy, M., Yuksel, S., 2013. Antimicrobial Photodynamic Therapy of Resistant Bacterial Strains by Indocyanine Green and 809-nm Diode Laser. Photomed. Laser Surg. 31, 155–162. https://doi.org/10.1089/pho.2012.3430.

Wang, B., Zhang, W., Pan, Q., Tao, J., Li, S., Jiang, T., Zhao, X., 2023. Hyaluronic Acid-Based CuS Nanoenzyme Biodegradable Microneedles for Treating Deep Cutaneous Fungal Infection without Drug Resistance. https://doi.org/10.1021/acs.nanolett.2c04539.

Wang, J., Koseki, S., Chung, M.J., Oh, D.H., 2017. A novel approach to predict the growth of Staphylococcus aureus on rice cake. Front. Microbiol. 8, 1–10. https://doi.org/10.3389/fmicb.2017.01140.

Wu, H., Or, V.W., Gonzalez-Calzada, S., Grassian, V.H., 2020. CuS nanoparticles in humid environments: adsorbed water enhances the transformation of CuS to CuSO4. Nanoscale 12, 19350–19358. https://doi.org/10.1039/D0NR05934J.

Xiang, Y., Mao, C., Liu, X., Cui, Z., Jing, D., Yang, X., Liang, Y., Li, Z., Zhu, S., Zheng, Y., Yeung, K.W.K., Zheng, D., Wang, X., Wu, S., 2019. Rapid and Superior Bacteria Killing of Carbon Quantum Dots/ZnO Decorated Injectable Folic Acid-Conjugated PDA Hydrogel through Dual-Light Triggered ROS and Membrane Permeability. Small 15, 1900322. https://doi.org/10.1002/smll.201900322.

Youf, R., Müller, M., Balasini, A., Thétiot, F., Müller, M., Hascoët, A., Jonas, U., Schönherr, H., Lemercier, G., Montier, T., Le Gall, T., 2021. Antimicrobial Photodynamic Therapy: Latest Developments with a Focus on Combinatory Strategies. Pharmaceutics. https://doi.org/10.3390/pharmaceutics13121995.

Yurtdaş-Kırımlıoğlu, G., Görgülü, Ş., 2021. Surface modification of PLGA nanoparticles with chitosan or Eudragit® RS 100: Characterization, prolonged release, cytotoxicity, and enhanced antimicrobial activity. J. Drug Deliv. Sci. Technol. 61, 102145. https://doi.org/10.1016/j.jddst.2020.102145.

Yus, C., Arruebo, M., Irusta, S., Sebastián, V., 2020. Microflow nanoprecipitation of positively charged gastroresistant polymer nanoparticles of Eudragit® RS100: A study of fluid dynamics and chemical parameters. Materials (basel). 13. https://doi.org/10.3390/ma13132925.

Zhang, Y., Yang, S., Wang, J., Cai, Y., Niu, L., Liu, X., Liu, C., Qi, H., Liu, A., 2021. Talanta Copper sulfide nanoclusters with multi-enzyme-like activities and its application in acid phosphatase sensing based on enzymatic cascade reaction. Talanta 233, 122594. https://doi.org/10.1016/j.talanta.2021.122594.